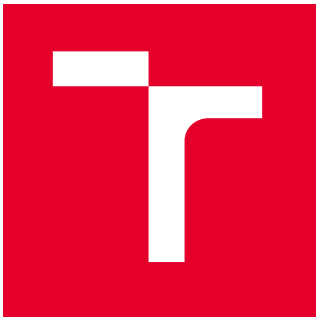


# BRNO UNIVERSITY OF TECHNOLOGY

VYSOKÉ UČENÍ TECHNICKÉ V BRNĚ

## FACULTY OF MECHANICAL ENGINEERING

FAKULTA STROJNÍHO INŽENÝRSTVÍ

## INSTITUTE OF PHYSICAL ENGINEERING

ÚSTAV FYZIKÁLNÍHO INŽENÝRSTVÍ


# DEVELOPMENT AND FABRICATION OF GRAPHENE HALL PROBES

VÝVOJ A VÝROBA GRAFENOVÝCH HALLOVÝCH SOND

**MASTER'S THESIS**

DIPLOMOVÁ PRÁCE


**AUTHOR** — **Bc. Linda Supalová**

AUTOR PRÁCE

**SUPERVISOR** — **doc. Ing. Miroslav Bartošík, Ph.D.**

VEDOUCÍ PRÁCE



**BRNO 2023**

BRNO UNIVERSITY OF TECHNOLOGY
FACULTY OF MECHANICAL ENGINEERING

# Assignment Master's Thesis

| | |
|---|---|
| Institut: | Institute of Physical Engineering |
| Student: | **Bc. Linda Supalová** |
| Degree programm: | Physical Engineering and Nanotechnology |
| Branch: | no specialisation |
| Supervisor: | **doc. Ing. Miroslav Bartošík, Ph.D.** |
| Academic year: | 2022/23 |

As provided for by the Act No. 111/98 Coll. on higher education institutions and the BUT Study and Examination Regulations, the director of the Institute hereby assigns the following topic of Master's Thesis:

## Development and fabrication of graphene Hall probes

**Brief Description:**

Due to the strong covalent bond of 7.6 eV between carbon atoms, graphene is a very stable material for electromagnetic applications with low temperature noise. As part of this diploma thesis, a graphene probe will be developed and manufactured for the detection of a magnetic field in the shape of a Hall bar using electron beam lithography (EBL). The probe will be tested for common neodymium magnets with a magnetic field in the order of hundreds of mT, while attention will be focused on the effect of temperature on the stability of the Hall voltage response, the possibility of amplifying the response by controlling the density of charge carriers through the gate voltage in a field controlled transistor (FET) arrangement, and the shape optimization of the probe.

**Master's Thesis goals:**

1. Do research on the mentioned issue.
2. Prepare suitable micrometer–sized Hall bars in a bottom solid–state gate FET arrangement.
3. Test the response of the Hall voltage to the magnetic field when changes:
a. the distance between the magnets (or the size of the applied magnetic field),
b. temperatures in the range of 25 to 200°C,
c. the concentration of charge carriers regulated by the lower gate.
4. Based on previous experience, optimize the design and other parameters of the probe for sufficient response.

**Recommended bibliography:**

COLLOMB, D., P. LI a S. BENDING. Frontiers of graphene-based Hall-effect sensors. Journal of Physics: Condensed Matter. 2021, 33(24). ISSN 0953-8984. doi: 10.1088/1361-648X/abf7e2

TANG, Chiu-Chun, Ming-Yang LI, L. J. LI, C. C. CHI a J. C. CHEN. Characteristics of a sensitive micro-Hall probe fabricated on chemical vapor deposited graphene over the temperature range from liquid-helium to room temperature. Applied Physics Letters. 2011, 99(11). ISSN 0003-6951. doi: 10.1063/1.3640218

DAUBER, Jan, Abhay A. SAGADE, Martin OELLERS, Kenji WATANABE, Takashi TANIGUCHI, Daniel NEUMAIER a Christoph STAMPFER, 2015. Ultra-sensitive Hall sensors based on graphene encapsulated in hexagonal boron nitride. Applied Physics Letters [online]. 106(19). ISSN 00036951. Dostupné z: doi:10.1063/1.4919897

NOVOSELOV, K S, Z JIANG, Y ZHANG, S V MOROZOV, H L STORMER, U ZEITLER, J C MAAN, G S BOEBINGER, P KIM a A K GEIM, 2007. Room-Temperature Quantum Hall. 315(March), 2007.

SCHAEFER, Brian T., Lei WANG, Alexander JARJOUR, Kenji WATANABE, Takashi TANIGUCHI, Paul L. MCEUEN a Katja C. NOWACK, 2020. Magnetic field detection limits for ultraclean graphene Hall sensors. Nature Communications [online]. 11(1), 1–8. ISSN 20411723. Dostupné z: doi:10.1038/s41467-020-18007-5

Deadline for submission Master's Thesis is given by the Schedule of the Academic year 2022/23

In Brno,

L. S.

prof. RNDr. Tomáš Šikola, CSc.
Director of the Institute

doc. Ing. Jiří Hlinka, Ph.D.
FME dean

## ABSTRACT

Advances in engineering and technology have created a demand for stable magnetic field detectors that are able to operate over a wide range of temperatures. At present, sensors based on the Hall effect and giant magnetoresistance effect are the most commonly used devices for real-time non-invasive measurement of both static and dynamic magnetic fields. Example applications of Hall effect-based devices include linear magnetic field sensors, gyrators, speed and directional sensors, electrical compasses, and current sensors, in areas ranging from manufacturing, automotive and aerospace to communication systems. However, currently used materials in Hall probes (mainly III-V semiconductors such as InSb or GaAs) struggle with temperature stability. In this study, we address the fabrication of Hall probes based on graphene and their testing at elevated temperatures. We successfully produce graphene Hall probes in a field effect transistor (FET) arrangement using standard fabrication techniques such as lithography and thin layer deposition. The choice of FET architecture allows us to take full advantage of the outstanding electronic properties of graphene during testing of the Hall probes from room temperature up to 200 °C. Our results reveal that increasing temperature does not cause significant degradation in the performance of graphene Hall probes even at temperatures above 150 °C. This work paves the way for future investigations into the behavior of graphene Hall probes at elevated temperatures, focusing on understanding the external factors that influence and impact the performance of the sensor in ambient conditions.



## KEYWORDS

graphene, Hall probe, Hall effect, field effect transistor, lithography



## ABSTRAKT

Pokrok v inženýrství a technologiích vytvořil zájem o stabilní detektory magnetického pole schopné operovat v širokém rozsahu teplot. Senzory založené na Hallově jevu a obří magnetorezistenci jsou nejčastěji využívaná zařízení k neinvazivnímu měření statických i dynamických magnetických polí v reálném čase. Aplikace zařízení na bázi Hallova jevu zahrnují například lineární senzory magnetického pole, gyrátory, rychlostní a směrové senzory, elektrické kompasy a senzory proudu, v oblastech sahajících od výroby, automobilového a kosmického průmyslu po komunikační systémy. Nicméně současné materiály využívané v Hallových sondách (především III-V polovodiče jako InSb nebo GaAs) mají potíže s teplotní stabilitou. V této práci se zabýváme výrobou Hallových sond založených na grafénu a jejich testováním za zvýšených teplot. Úspěšně jsme vyrobili grafénové Hallovy sondy v uspořádání polem řízeného tranzistoru pomocí standartních výrobních metod jako litografie a depozice tenkých vrstev. Volba uspořádání polem řízeného tranzistoru nám umožňuje naplno využít vynikajících elektrických vlastností grafénu při testování těchto Hallových sond v rozmezí od pokojové teploty až do 200 °C. Naše výsledky ukazují, že zvyšování teploty nezpůsobuje zásadní zhoršení výkonnosti grafénových Hallových sond i při teplotách nad 150 °C. Tato práce otevírá dveře pro další výzkum chování grafénových Hallových sond za zvýšené teploty s důrazem na porozumění externích faktorů, které ovlivňují výkonnost takového senzoru při využití v normálních podmínkách.



## KLÍČOVÁ SLOVA

gafén, Hallova sonda, Hallův jev, polem řízený tranzistor, litografie

SUPALOVÁ, Linda. *Development and fabrication of graphene Hall probes*. Brno: Brno University of Technology, Faculty of Mechanical Engineering, Department of Physical Engineering, 2023, 67 p. Master's Thesis. Supervised by doc. Ing. Miroslav Bartošík, Ph.D.

# Author's Declaration

| | |
|---|---|
| **Author:** | Bc. Linda Supalová |
| **Author's ID:** | 209477 |
| **Paper type:** | Master's Thesis |
| **Academic year:** | 2022/23 |
| **Topic:** | Development and fabrication of graphene Hall probes |

I declare that I have written this paper independently, under the guidance of the advisor and using exclusively the technical references and other sources of information cited in the paper and listed in the comprehensive bibliography at the end of the paper.

As the author, I furthermore declare that, with respect to the creation of this paper, I have not infringed any copyright or violated anyone's personal and/or ownership rights. In this context, I am fully aware of the consequences of breaking Regulation § 11 of the Copyright Act No. 121/2000 Coll. of the Czech Republic, as amended, and of any breach of rights related to intellectual property or introduced within amendments to relevant Acts such as the Intellectual Property Act or the Criminal Code, Act No. 40/2009 Coll. of the Czech Republic, Section 2, Head VI, Part 4.

Brno ..... .....

author's signature*

*The author signs only in the printed version.

# ACKNOWLEDGEMENT

Rád bych poděkoval vedoucímu bakalářské/diplomové/disertační práce panu Ing. XXX YYY, Ph.D. za odborné vedení, konzultace, trpělivost a podnětné návrhy k práci.

# Contents

# 1 Graphene among 2D materials

Graphene, an allotrope of carbon with a thickness of only one atomic layer, belongs to the novel family of layered two-dimensional materials that has been of increasing interest to the scientific community since Geim and Novoselov first isolated graphene monolayers almost two decades ago [1]. Materials in this group are characterized by strong covalent in-plane bonding and weak van der Waals coupling between individual layers. Other prominent representatives of this group include *transition metal dichalcogenides* (TMDCs), *hexagonal boron nitride* (hBN), and black phosphorus (phosphorene).

Approaching the 2D limit, these materials acquire unique electronic [2], optical [3] and mechanical [4] properties that are missing in their bulk counterparts. For example, group VI TMDCs such as $MoS_2$, $MoSe_2$, $WSe_2$, and $WS_2$, undergo a transition from indirect to direct band gap semiconductors when thinned down to a monolayer and exhibit strong excitonic effects such as bright photoluminescence (PL) [5] and spin-valley coupling [6]. In addition, 2D materials resist in-plane deformations due to their structure and can endure relatively large strain before breaking. This makes strain engineering a viable option to modulate their band gap, charge carrier mobility, thermal conductivity, and dielectric properties [7]. Graphene, in particular, exhibits gas impermeability [8], high in-plane thermal conductivity of $5\,000\,\mathrm{WmK}^{-1}$ [9] and large light transmittance of $\sim 97.7\,\%$ in the infrared region [10].

## 1.1 Structure and electronic properties of graphene

A single layer of graphene consists of carbon atoms arranged in a hexagonal (honey-comb) lattice with a unit cell formed by two carbon atoms, A and B, separated by a distance $a \approx 1.42\,\text{Å}$ (Fig. 1.1a). However, the unique electronic properties of graphene arise at the so-called Dirac points, which are the points $K$ and $K'$ at the corners of the first Brillouin zone in the reciprocal space, Fig. 1.1b.

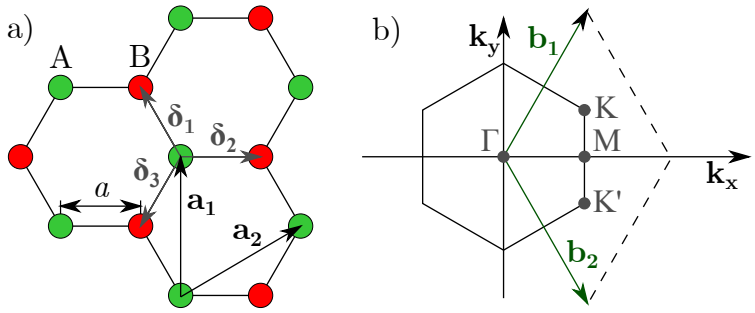


**Fig. 1.1:** a) The graphene lattice showcases the carbon-carbon distance $a$, the lattice primitive vectors $\mathbf{a_1}, \mathbf{a_2}$ and the nearest neighbour vectors $\boldsymbol{\delta_i}$ $(i = 1, 2, 3)$. b) First Brillouin zone of the reciprocal lattice with the reciprocal lattice vectors $\mathbf{b_1}, \mathbf{b_2}$ and the so-called Dirac points $K$ and $K'$. Adapted from [11].

In fact, graphene represents the $sp^2$ hybridization of carbon, Fig. 1.2. The strength of its lattice comes from the covalent $\sigma$ bonds between the $sp^2$ orbitals of neighbouring atoms. As a matter of fact, each atom contributes three of its four valence electrons to these bonds and the fourth electron belongs to the $p_z$ orbital, which is perpendicular to the plane of the monolayer. In this way, the $p_z$ orbitals form delocalized $\pi$ bands above

and below the lattice plane, which enable an easy flow of electrons through the material, leading to high conductivity and semimetallic behaviour.

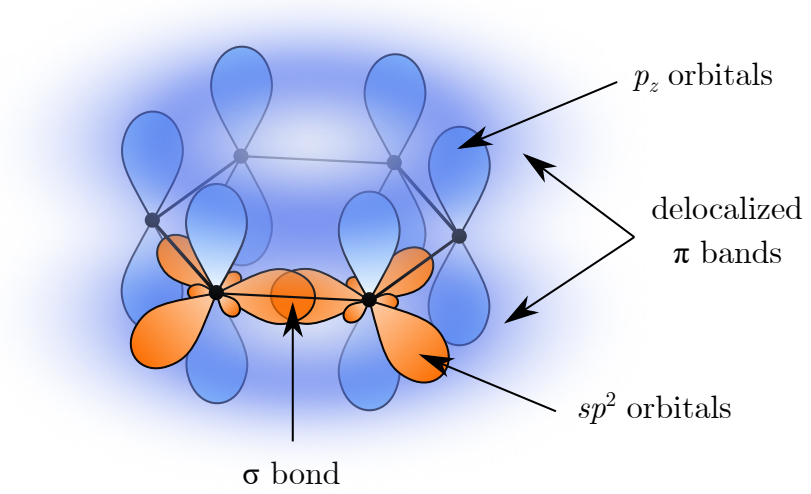


**Fig. 1.2:** A ring of carbon atoms in the $sp^2$ hybridization. The three hybridized $sp^2$ orbitals (orange, shown only for the two foremost atoms for clarity) lie in the plane of the graphene lattice, forming σ bonds in the overlaps of neighbouring orbitals. Perpendicular to the graphene layer stand the $p_z$ orbitals (blue), which form the delocalized π bands.

As we can see in Fig. 1.3, the valence π band and the conduction π* band meet at the aforementioned Dirac points *K* and *K'* of the Brillouin zone, making graphene a zero band gap semiconductor. Yet, chemical doping [13], lithographic patterning [14], and the influence of the substrate [15] have all been used to experimentally produce a band gap in graphene. In general, any disruption to the symmetry of the graphene structure can cause the formation of a band gap. Specifically, the cone shape of the valence and conduction bands around the Dirac points is the main point of symmetry, which results in a linear

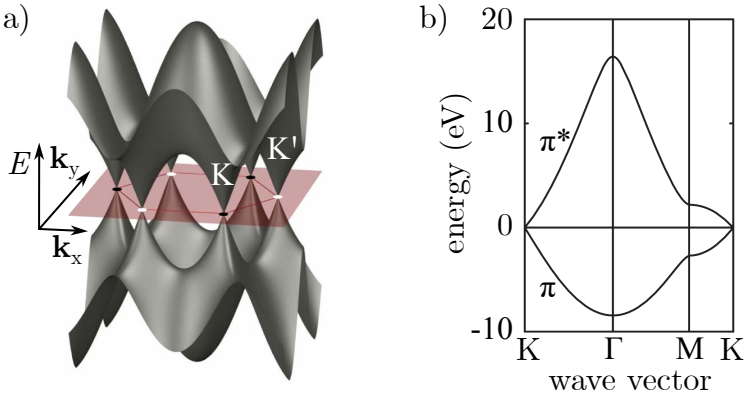


**Fig. 1.3:** The band structure of graphene. a) The energy spectrum in the reciprocal space with the valence and conduction bands meeting at the Dirac points *K* and *K'*. b) The dispersion relation of the π bands in the first Brillouin zone. Adapted from [12, 16].

dispersion relation $E = \pm v_F|\mathbf{k}|$ [11], in contrast to the parabolic dispersion relation found in conventional semiconductors. The linear dispersion relation of graphene close to the Dirac point is similar to the linear dispersion relation of relativistic massless particles like photons ($E = \sqrt{p^2c^2 + {m_0}^2c^4}$, where $m_0 = 0$). Nonetheless, charge carriers in graphene have a non-zero mass and are thus moving at the Fermi velocity $v_F \approx 10^6\,\mathrm{ms}^{-1}(\ll c)$. To concisely explain all these facts, it is suggested that the charge carriers in graphene behave as massless Dirac fermions.

In pristine graphene, the Fermi level $E_F$ intersects the Dirac point. This corresponds to the state of minimal conductivity as electrons and holes are in equilibrium. In theory, the minimal conductivity in graphene is predicted to be $4e^2/\pi h$ [17], where $e$ represents the elementary charge and $h$ the Planck constant. However, experimentally measured values differ and the lowest reported values approach $(1 \div 4)\, e^2/h$ [18–20]. This discrepancy can be attributed to the presence of scattering sources, such as intrinsic charged point defects in graphene, defects in the substrate (e.g. in $SiO_2$), and trapped charges at the interface between graphene and the substrate [21].

Furthermore, tuning the Fermi level by doping can continuously invert the majority charge carriers in graphene from electrons to holes and vice versa. This ambipolar behaviour can be achieved through various means, for instance by the application of an external electric field [22], adsorption of atoms or molecules on the surface [23, 24], or substituting carbon atoms with heteroatoms in the graphene lattice [25, 26]. As a matter of fact, the controlled doping of graphene is crucial for sensor applications, as it can significantly enhance device sensitivity [27].

## 1.2 Synthesis methods

Various methods have been developed over the years to obtain mono- and few-layer 2D materials, falling into both top-down and bottom-up categories. Top-down methods start with bulk materials that are gradually reduced to the desired 2D structure. However, not all 2D materials necessarily exist in bulk form. To synthesize such structures, bottom-up methods are employed, building up the 2D material from individual atoms. In the case of graphene, both top-down and bottom-up techniques are applicable and the most commonly used methods are mechanical exfoliation, epitaxial growth by thermal decomposition of *silicon carbide* (SiC), and *chemical vapour deposition* (CVD).

The simplest method to obtain high-quality mono- and few-layer graphene flakes on any substrate is mechanical exfoliation, as it requires only quality bulk graphite, adhesive tape and an optical microscope. In short, graphite crystals are thinned down to the monolayer by repeated use of adhesive tape, and graphene flakes are subsequently identified based on their optical contrast. Although easy to learn, mechanical exfoliation is a cumbersome, labour-intensive process due to the time-consuming search for suitable flakes and the lack of control over the size and distribution of graphene layers. Despite its limitations preventing large-scale industrial use, it is still widely used to prototype research devices, even with alternative synthesis methods available.

In contrast, epitaxial growth of graphene by thermal decomposition of SiC offer potential as a promising synthesis method for use in high-end electronics that could surpass current silicon-based devices in terms of speed, feature sizes, and power consumption [28]. In brief, bulk SiC is annealed at high temperatures (usually over 1400,° C) in a high vacuum environment, causing the thermal decomposition of SiC, which leads to the evaporation of Si atoms and the formation of a graphitic layer on the surface. The quality

and electronic properties of this graphitic layer can vary based on the underlying SiC crystal and growth conditions, resulting in outcomes ranging from a nearly free-standing graphene layer to a polycrystalline graphene multilayer [29]. Nonetheless, the use of SiC substrate in this method is a major disadvantage, as it is not universally suitable for all applications.

Unlike epitaxial growth of graphene on SiC, chemical vapour deposition produces large-area graphene sheets that can be transferred onto any arbitrary substrate, making CVD graphene highly suitable for a wide range of applications.

During CVD, a hydrocarbon precursor gas reacts with or thermally decomposes on the substrate at high temperature. The exact growth parameters depend on several factors, such as the choice of the precursor gas, substrate, or CVD furnace construction. For instance, the most common precursors are methane and ethylene, but any organic substance can be used in theory [30]. In addition, various metals have been tried as substrates for CVD growth of graphene, mainly transition metals such as Cu [31–34], Ni [35], Pt [36], Ir [37], Co [38], and Pd [39]. Copper films have received the most attention as growth substrates due to the extremely low solubility of carbon in copper, which promotes uniform monolayer growth under the right conditions.

The initial step in graphene growth involves annealing the substrate at a high temperature (typically $\approx 1000\,^{\circ}\mathrm{C}$), prior to introducing the precursor gas into the growth chamber. For most metals, the carbon atoms from the precursor dissolve into the substrate and later diffuse out again to precipitate on the surface as the sample cools down, Fig. 1.4a. However, the mechanism works differently on copper because carbon atoms accumulate on the surface after the hydrocarbon decomposition rather than diffuse into the substrate bulk, Fig. 1.4b. In fact, the carbon atoms on the copper foil surface begin to form growth centres, which then expand into grains that grow in size until connecting with neighbouring grains. At this stage, a monolayer of graphene completely covers the Cu surface, with no exposed catalyst remaining to promote further growth. Clearly, this self-regulated monolayer growth is a key advantage of using copper foil as the substrate. Nevertheless, multilayers can form if the growth rate is too fast. In that case, the second and third layers emerge at the original growth centres before the whole Cu surface is covered by the monolayer.

Graphene grown via CVD is usually polycrystalline, made of a patchwork of grains with

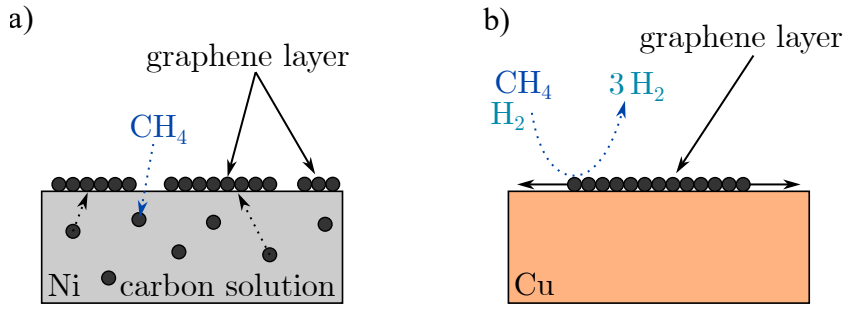


**Fig. 1.4:** Graphene growth mechanism on Ni and Cu substrates. a) Carbon atoms from the precursor gas (methane) dissolve into the Ni substrate, forming a carbon solution at high temperatures. During coolling, the carbon atoms diffuse out of the substrate and onto the surface, where they form graphene layers. b) When methane is catalytically decomposed on the Cu substrate, carbon atoms accumulate on the surface and grow into a single layer from initial nucleation sites. Adapted from [40].

varying sizes and orientations, stitched together by irregularly-shaped grain boundaries [41]. As a matter of fact, these grain boundaries are the origins of scattering and defects in graphene, which impedes its electronic properties by increasing the resistivity of regions containing said boundaries [42]. Although it is possible to grow graphene monocrystals using CVD by controlling the number of nucleation sites [43, 44], it takes a long time to grow a single graphene grain to a massive size (e.g. 12 hours for grains with a size of several millimetres). Nonetheless, Petrone et al. showed that CVD graphene with large grain size (up to 250 µm) exhibits quality comparable to exfoliated graphene based on low-temperature electrical transport and magnetotransport measurements [45].

# 2 Hall probes

Hall probes are nowadays a ubiquitous type of sensor, which has found its place in areas ranging from automotive and manufacturing to aerospace and communication systems. Together with sensors based on the giant magnetoresistance effect, Hall probes are the most commonly used devices for real-time non-invasive measurement of both static and dynamic magnetic fields. Example applications of Hall effect-based sensors include electrical compasses, gyrators, vane sensors, linear magnetic field sensors, current sensors, position, speed and directional sensors [46, 47], just to mention a few. In many of these applications, there is a demand for low-cost, small-sized sensors able to operate efficiently over a range of magnetic fields and temperatures.

One of the advantages of these sensors is the possibility to integrate the Hall effect-based elements with interfacing electronics on a single chip, opening the way for compact, versatile, small-scale devices. As a matter of fact, high-end commercial Hall sensors all consist of a central Hall element and silicon *complementary metal-oxide-semiconductor* (CMOS) processing integrated circuits, which improve the performance of the whole sensor several times [48]. As the Hall element translates a magnetic field into an electrical signal, this analog signal is usually amplified by a preamplifier before being converted by an analog-to-digital converter to a digital signal, which can be further processed by other circuits. Additionally, the Hall elements can also be fabricated in the micro- to nano-scale, satisfying the industry-wide desire for miniaturization.

## 2.1 Hall effect

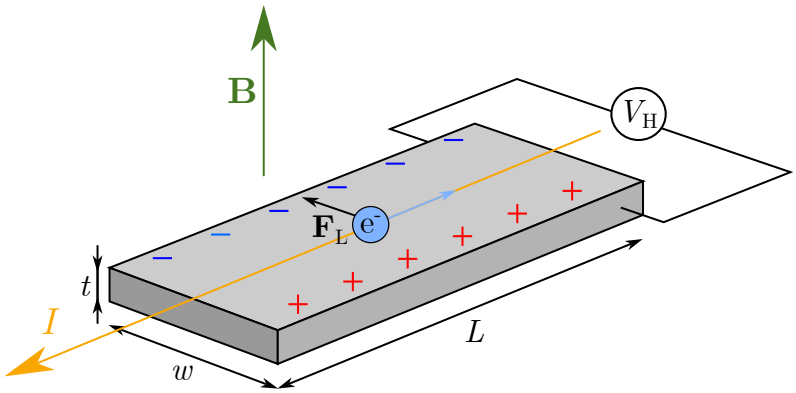


**Fig. 2.1:** Schematic illustration of the Hall effect. Current $I$ flowing through a conductive strip with width $w$, length $L$, and thickness $t$, placed in an out-of-plane magnetic field $\mathbf{B}$, causes the deflection of electrons $e^-$ to the sides of the strip, resulting in a potential difference across the width of the strip, which can be experimentally measured as the Hall voltage $V_H$.

As the name suggests, Hall probes are based on the well-known Hall effect, which describes the formation of a potential difference in a conductive strip placed in a transverse magnetic field with current flowing through the strip, Fig. 2.1. The charge carriers are acted upon by the Lorentz force

$$\mathbf{F}_L = q(\mathbf{E} + \mathbf{v} \times \mathbf{B}), \tag{2.1}$$

where $q$ is the charge of the carriers, $\mathbf{E}$ is the electric field, $\mathbf{v}$ is the carrier drift velocity and $\mathbf{B}$ is the magnetic field. In the case of the Hall effect, we consider the external electric field equal to zero and the magnetic field perpendicular to the flow of charge carriers. The trajectory of the charge carriers is going to be curved to one side by the Lorentz force, creating a charge imbalance between the sides of the strip. This transverse potential difference creates an internal electric field whose force $\mathbf{F}_{\mathrm{E}}$ balances the Lorentz force under steady state condition so that

$$\mathbf{F} = \mathbf{F}_{\mathrm{L}} + \mathbf{F}_{\mathrm{E}} = \mathbf{0}. \tag{2.2}$$

Considering that the magnetic field $\mathbf{B}$ is perpendicular to the induced electric field $\mathbf{E}$, the steady state condition can be rewritten into:

$$0 = E - vB. \tag{2.3}$$

Next, the induced electric field $E$ and the driving current $I$ can be defined as:

$$E = \frac{V_{\mathrm{H}}}{w}, \tag{2.4}$$

$$I = n \cdot w \cdot t \cdot v \cdot q, \tag{2.5}$$

where $V_{\mathrm{H}}$ is the Hall voltage, $n$ is the carrier density, $w$ and $t$ are the width and the thickness of the conductive strip. The transverse (Hall) voltage can be subsequently expressed as

$$V_{\mathrm{H}} = \frac{BI}{ntq}. \tag{2.6}$$

Specifically for 2D materials such as graphene, the thickness $t$ of the material is suppressed and the carrier density $n$ is then replaced by 2D carrier density $n_{2\mathrm{D}} \equiv nt$, so that the Hall voltage transforms into

$$V_{\mathrm{H}} = \frac{BI}{n_{2\mathrm{D}}q}. \tag{2.7}$$

At low temperatures and high magnetic fields, quantum phenomena appear in 2D materials and the Hall voltage shows a step-like increase with increasing magnetic field. This so-called *quantum Hall effect* (QHE) has been observed in graphene also at room temperature [51], however, the study required a magnetic field of almost 30 T.

The classical linear dependence of the Hall voltage $V_{\mathrm{H}}$ on the applied magnetic field $B$ and the driving current $I$ predisposes Hall effect-based sensors for frequent and simple use in a wide range of applications, as was already mentioned at the beginning of this chapter. However, the choice of the optimal working material of the Hall probe is essential as a result of the Hall voltage $V_{\mathrm{H}}$ dependence on the material properties, namely the charge carrier density $n$ and the related charge carrier mobility $\mu$. Currently, the majority of Hall elements are based on thin layers of either silicon or III-V semiconductors, such as InSb and GaAs. The main advantage of silicon is the easy implementation in CMOS processes used for the manufacturing of integrated Hall sensors. Yet, its mediocre material properties are detrimental to the overall performance of these Hall probes. Although III-V semiconductors exhibit higher charge carrier mobility compared to silicon, these materials face issues in high-temperature applications.

In fact, the intrinsic charge carrier density $n_0$ of semiconductors increases with rising

temperature $T$ [49] as

$$n_0 \propto T^{3/2} \cdot \exp\left(-\frac{E_g}{2k_B T}\right), \tag{2.8}$$

where $E_g$ is the band gap energy and $k_B$ is the Boltzmann constant. As a result, the Hall voltage response rapidly decreases with increasing temperature per eq. 2.6. In contrast, the 2D charge carrier density $n_{2D}$ in graphene is independent of temperature [50] and the mobility $\mu$ of high-quality graphene also retains higher values at various temperatures compared to semiconductors [52]. In addition, monolayer graphene represents the limit case of decreasing the thickness $t$ of the working material of the Hall element to increase its Hall voltage response $V_H$.

To summarize, graphene clearly avoids the shortcomings of traditional semiconductors for usage as Hall elements, while possessing the most suitable material properties to take advantage of the Hall effect. Furthermore, the performance of the graphene Hall elements can be enhanced by employing the *field effect transistor* (FET) architecture to tune the charge carrier density by changing the doping level.

## 2.2 Graphene field effect transistors

In general, a field effect transistor consists of source and drain electrodes, which are connected by a channel region, and a gate electrode, which is separated from the conductive channel by an insulating barrier. Specifically for graphene FETs, the most common configuration employs a solid-state back gate, Fig. 2.2a. In principle, the basic operation of FET relies on controlling the conductivity of the channel by applying gate voltage. In this regard, graphene FETs function just as classical FETs utilizing semiconductor materials in the conductive channel. The field effect changes the sheet conductivity of the graphene channel by modulating its Fermi level $E_F$ so that the sheet conductivity $\sigma_s$ (or inversely, the sheet resistivity $\rho_s = \sigma_s^{-1}$) roughly follows the conical shape of the band structure.

The type and density of charge carriers are determined by the potential difference between the gate and the channel with regard to the initial doping of the graphene layer. For instance, even the application of a small positive gate voltage to an undoped graphene layer causes electrons to accumulate, which results in the n-doping of the graphene channel, Fig. 2.2b. However, if the graphene layer is originally heavily p-doped, the application of a small positive bias only partially compensates the p-doping and a large positive gate voltage is necessary to change the majority charge carriers in the graphene channel to electrons, Fig. 2.2c. Therefore, the initial doping of the graphene layer is the determining factor for the utility of the field effect in probing the ambipolar behaviour of graphene.

The most important part of the conductivity (resistivity) modulation by the field effect concerns the crossing of the Fermi level through the point of contact between the valence and conduction bands in graphene when the charge carriers are in equilibrium. Due to the crossing of the Dirac point in the band structure, the corresponding gate voltage $V_G$ is accordingly called the Dirac point voltage $V_D$, although the term *charge neutrality point* is occasionally used instead in the literature [47, 68, 73] and the gate voltage is then denoted as $V_{CNP}$. In fact, the most interesting physics happens around the Dirac point and the Hall effect in graphene is no exception.

The Hall voltage $V_H$ is inversely proportional to the 2D charge carrier density $n_{2D}$ (eq. 2.7), which can be related to the applied gate voltage in a graphene FET with respect to

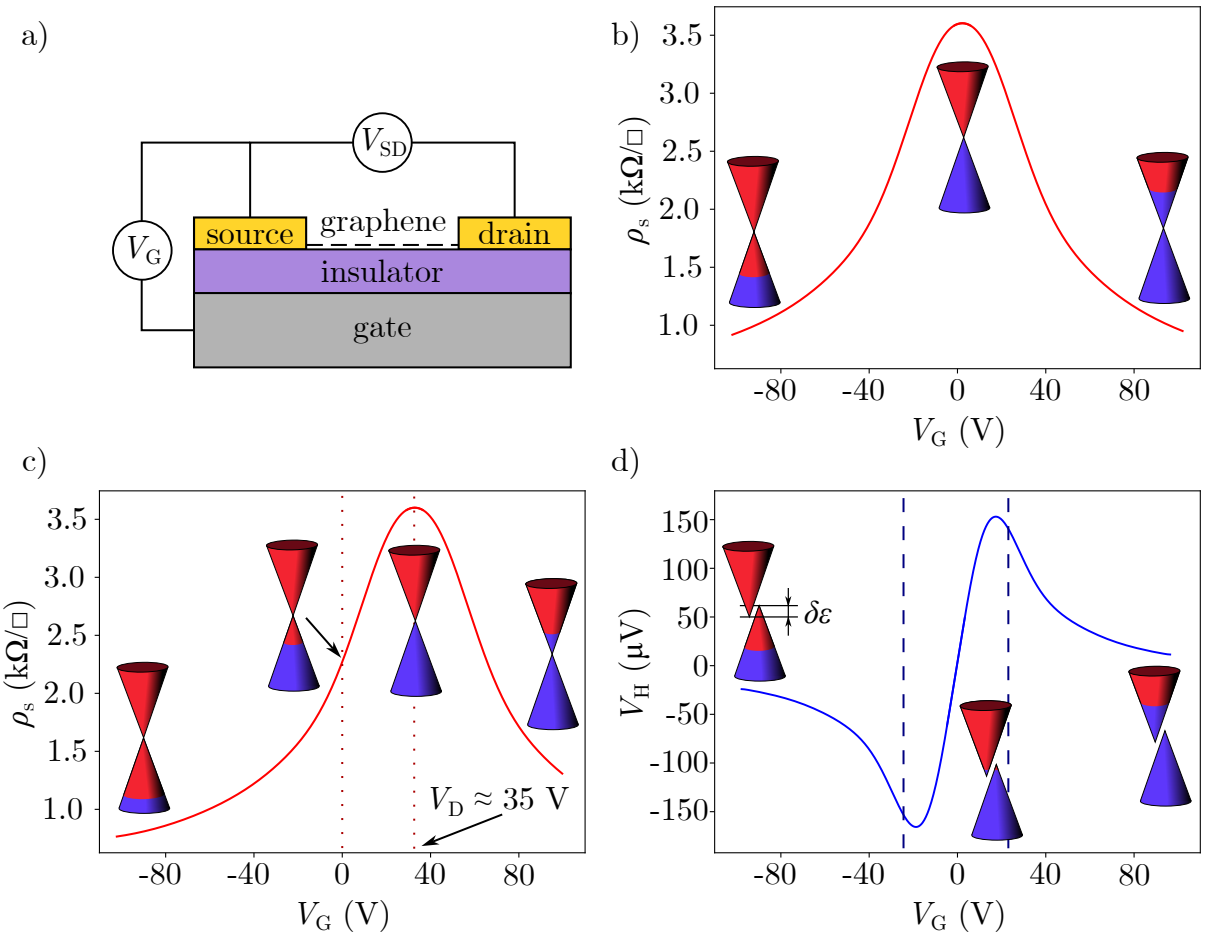


**Fig. 2.2:** Field effect modulation of graphene. a) Scheme of a solid-state back gate graphene FET. The application of back gate voltage between the gate and source electrodes controls the conductivity (resistivity) of the graphene channel between the source and drain electrodes. b) Transfer curve $\rho_s(V_G)$ of the intrinsic graphene channel. The sheet resistivity $\rho_s$ is invariant to scaling and depends only the width/length ratio of the graphene layer. The doping level of graphene for different parts of the transfer curve is illustratively marked by the conical band structure with the Dirac point voltage corresponding to $V_G = 0\,\mathrm{V}$. c) Transfer curve $\rho_s(V_G)$ of an initially p-doped graphene channel, which is illustrated by the prevalence of holes in the band structure at $V_G = 0\,\mathrm{V}$ and the Dirac point voltage $V_D$ located at $V_G \sim 35\,\mathrm{V}$. d) Dependence of the Hall voltage $V_H$ on the applied gate voltage $V_G$ for an undoped graphene layer, e.g. $V_D = 0\,\mathrm{V}$ as in b). Far away from the Dirac point, $V_H \propto {V_G}^{-1}$, however, there is a transition period around the Dirac point (between the dashed lines) where the Hall voltage response depends on the difference in electron and hole concentrations, which can be explained by considering a small overlap $\delta\varepsilon$ between the valence and conduction bands.

any initial doping by using the parallel-plate capacitor model:

$$n_{2D} = \frac{\varepsilon_0 \varepsilon_r}{qd}(V_D - V_G), \tag{2.9}$$

where $\varepsilon_0$ is the permittivity of vacuum, $\varepsilon_r$ and $d$ are the relative permittivity and thickness of the isolating layer.

Fig. 2.2d depicts the typical dependency of Hall voltage $V_H$ on gate voltage $V_G$ in a graphene FET. Far away from the Dirac point, the Hall voltage follows the ${n_{2D}}^{-1} \propto (V_D - V_G)^{-1}$ dependence both for electrons and holes. However, the Hall voltage response reaches its peak value for both types of carriers for gate voltages slightly away from the Dirac point voltage with a transition period between the two extremes. During this transition, the Hall voltage decreases and actually crosses zero at the Dirac point, even though the charge carrier density reaches its minimum. An explanation for this discrepancy has been proposed by Novoselov and Geim [1] by accounting for a small overlap $\delta\varepsilon$ between the conduction and valence bands. In the transition period, one type of carrier is substituted by another, which is also supported by the relatively small change of resistivity $\rho$ with gate voltage $V_G$. The Hall voltage is then proportional to the difference between electron and hole concentrations in this transition state. In short, the application of gate voltage divides the Hall voltage response into three parts, two of which are fully occupied either by holes or electrons and follow the usual $V_H \propto {n_{2D}}^{-1}$ dependency, and a transition period, in which both types of carriers are present and the Hall voltage $V_H$ reflects the inequality between electron and hole concentrations.

## 2.3 Graphene Hall probes

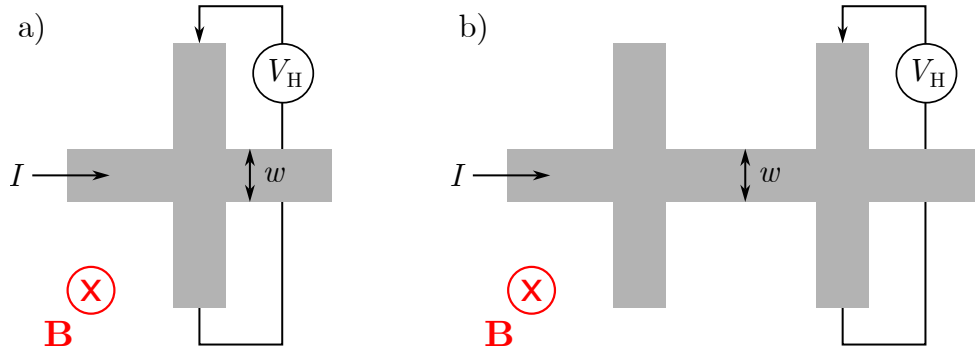


**Fig. 2.3:** Graphene geometries for the measurement of the Hall effect. a) Hall cross, the simplest geometry of Hall probes. b) Multi-terminal Hall bar, commonly with two or more pairs of opposing electrodes for the measurement of $V_H$. In both cases, the main parameters are the width of the main channel $w$, the driving current $I$, and the applied magnetic field $\mathbf{B}$.

The concept of a functional Hall probe based on graphene has already been proved many times for low- to room-temperature measurements, utilizing graphene layers prepared by different synthesis methods commonly patterned into either a Hall cross or a Hall bar geometry, Fig. 2.3. To assess the sensitivity of the Hall probe, the Hall coefficient $R_H$ is defined as:

$$R_H = \frac{1}{I}\frac{\partial V_H}{\partial B}. \tag{2.10}$$

In addition, it is necessary to take into account the electronic noise which limits the

detection capabilities of the Hall probe and defines the magnetic field detection limit [74]:

$$S_{\mathrm{B}}^{1/2} = \frac{S_{\mathrm{V}}^{1/2}}{I R_{\mathrm{H}}}, \tag{2.11}$$

where $S_{\mathrm{V}}^{1/2}$ is the frequency-dependent Hall voltage noise. In particular, the "$1/f$" flicker noise sets a lower limit for the noise spectrum at low frequencies and the choice of operation frequency can alter the detection limit by an order of magnitude [74].

A summary of graphene Hall probes reported in the literature is presented in Tab. 2.1 along with a comparison to semiconductor-based Hall probes. Given the influence of charge carrier density in graphene on the Hall voltage response of the sensor, graphene Hall probes in the FET configuration are denoted as "Hall probes with field effect modulation" and the reported sensitivities are the best results that can be achieved with control of the graphene conductivity by applying gate voltage. In contrast, graphene Hall probes without this option are dependent on the cleanliness of the graphene layer and any residual doping from fabrication processes can be detrimental to the sensor performance. Although many of the graphene Hall probes were also tested at low temperatures, the focus of this work is on the room- to high-temperature range, therefore only results reported at room temperature and above are chosen for comparison.

There are several trends which can be seen from the performance of various Hall probes based on graphene synthesized by different methods and patterned into Hall elements in a wide range of sizes. Regardless of the synthesis method, graphene Hall probes either surpass or at least show comparable sensitivity to semiconductor Hall probes. Generally, smaller width of the graphene channel $w$ worsens the magnetic field detection limit $S_{\mathrm{B}}^{1/2}$, as the presence of graphene edges causes scattering of electrons and increases the electronic noise in the device, which is especially notable for sub-micron graphene channels [68]. Even though the sensitivity as defined by the Hall coefficient $R_{\mathrm{H}}$ is normalized to remove the influence of the driving current $I$ (eq. 2.10), the usage of a higher current is associated with a better signal-to-noise ratio and a necessary condition for commercial applications. Furthermore, it has been shown that graphene encapsulation in hBN significantly improves the Hall probe performance [57, 74, 75], however, the main method for obtaining such samples uses stacking of exfoliated flakes of hBN and graphene, which is incompatible with large-scale industrial production. Besides hBN, dielectrics (such as $Al_2O_3$ [64, 70]) and polymer-based resists (for example PMMA [48, 57], SU-8 [69], and co-polymers [63]) have also been tried as passivation layers on top of the graphene channel, although none proved as consequential as hBN. Nonetheless, the use of a passivation layer is still beneficial as it isolates the graphene layer from any environmental influences (e.g. doping from the adsorption of water molecules). In this regard, the addition of a passivation layer enhances the stability of the sensor.

In conclusion, it has been established that graphene is an attractive substitute for semiconducting materials in Hall probes due to its outstanding electronic properties, which translate into enhanced sensitivity and detection limit. In fact, Dai et al. demonstrated that combining a graphene Hall element with standard CMOS integrated circuits further increased the sensitivity from 1 kΩ/T to 64 kΩ/T, which surpassed even high-end commercial Hall probes [48]. Additionally, studies have shown that the sensitivity of graphene Hall probes is stable over a wide range of temperatures [59, 64]. However, none of them utilized the FET configuration to properly explore the limits of graphene Hall probes at high temperatures by fine-tuning the electronic properties of the graphene channel.

**Tab. 2.1:** Summary of graphene Hall probes reported in the literature with comparison to Hall probes based on other materials. The main characteristics are the Hall coefficient $R_H$ and the magnetic field detection limit $S_B^{1/2}$. When applicable, supplementary parameters include the width of the main channel of the Hall element $w$, the measurement bandwidth $f$, the driving current $I$ and the measurement temperature $T$.

**Hall probes without field effect modulation**

| channel material | $R_H$ ($\Omega$/T) | $S_B^{1/2}$ ($\mu$T/$\sqrt{\text{Hz}}$) | $f$ (kHz) | $I$ ($\mu$A) | $w$ ($\mu$m) | $T$ (K) |
|---|---|---|---|---|---|---|
| CVD graphene [48] | 1000 | 20 | 0.2 | 100 | 20 | 300 |
| CVD graphene [53] | 2093 | 0.1 | 3 | 200 | 50 | 300 |
| CVD graphene [54] | 500 | 0.7 | 3 | 100 | 60 | 300 |
| CVD graphene [55] | 1800 | 20 | 1 | 3 | 1 | 300 |
| CVD graphene [56] | 2540 | 0.162 | 2 | 15 | 10 | 300 |
| CVD graphene [57] | 2270 | - | - | 30 | 12 | 300 |
| CVD graphene [58] | 575 | - | - | 100 | 2 | 400 |
| CVD graphene [59] | 40 | - | - | 3 000 | - | 300–473 |
| epitaxial graphene [60] | 1442 | 0.047 | 3 | 400 | 30–140 | 300 |
| | 300 | 0.1 | 3 | 400 | 30–140 | 423 |
| epitaxial graphene [61] | 790 | 2.5 | 3.3 | 10 | 10 | 300 |
| epitaxial graphene [62] | 1250 | 1.6 | 80 | 20 | 1 | 300 |
| epitaxial graphene [63] | 1615 | 60 | 0.001 | 50 | 0.5 | 300 |
| epitaxial graphene [64] | 80 | - | - | 1 000 | 100 | 300–573 |
| exfoliated graphene [65] | 700 | 54 | 1 | 0.5 | 1 | 300 |
| InAs/GaSb [66] | 537 | 0.5 | 3 | 100 | 60 | 300 |
| AlGaN/GaN [67] | 77 | - | - | 100 | 5 | 300–673 |
| AlGaAs/GaAs [67] | 340 | - | - | 5 | 5 | 300 |
| InAsSb quantum well [67] | 2750 | - | - | 50 | 50 | 300 |

**Hall probes with field effect modulation**

| channel material | $R_H$ ($\Omega$/T) | $S_B^{1/2}$ ($\mu$T/$\sqrt{\text{Hz}}$) | $f$ (kHz) | $I$ ($\mu$A) | $w$ ($\mu$m) | $T$ (K) |
|---|---|---|---|---|---|---|
| CVD graphene [58] | 1550 | 0.8 | 3 | 100 | 2 | 300 |
| CVD graphene [68] | 140 | 59 | 0.531 | 12 | 0.085 | 300 |
| CVD graphene [69] | 1000 | 0.5 | 3 | 100 | 15 | 300 |
| CVD graphene [70] | 1076 | 1.16 | 1 | 500 | 25 | 300 |
| CVD graphene [71] | 345 | - | - | 15 | 0.5 | 300 |
| CVD graphene [72] | 1200 | 43 | 50 | 3 | 5 | 300 |
| CVD graphene [73] | 464 | - | - | 1 | 30 | 300 |
| exfoliated graphene [74] | 6 840 | 0.7 | 1 | 50 | 1 | 300 |
| exfoliated graphene [75] | 5 700 | 0.05 | 3 | 5 | 3 | 300 |

# 3 Hall probe design & fabrication

As with any electronic device, the appropriate design is essential to reach the peak performance of a graphene Hall probe. This encompasses everything from the choice of the materials to the dimensions and layout of the individual parts, including any application-specific optimizations. Especially for graphene Hall probes, the quality of the graphene layer is the main determining factor for the sensitivity, which sets an upper limit to the capabilities of the sensor. However, other parameters (for instance the shape of the graphene channel) need to be also taken into account given the detrimental effect of electronic noise in the device on the detection limit. Hence, we choose to fabricate Hall probes with CVD graphene in the FET configuration utilizing standard lithographic processes based on the available research in the literature and with the intended high-temperature applications in mind.

## 3.1 Design of the sensor

Due to the overall complexity of the graphene Hall probe, there are several aspects to the final design (Fig. 3.1) that are worth highlighting and explaining.

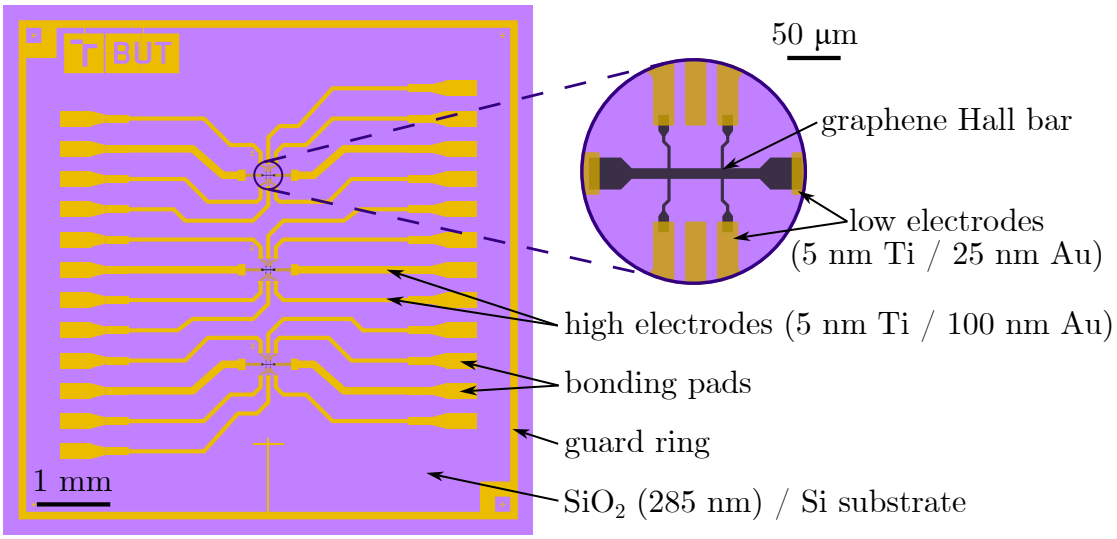


**Fig. 3.1:** Design of the graphene Hall probe. The substrate is a silicon chip with a $SiO_2$ insulation layer, which acts as a global back gate. Every chip contains three Hall bar positions and a guard ring around the edge to remove the influence of external electric fields. The graphene Hall bar (shown in the detail) is contacted by two-step gold electrodes with bonding pads at the end for subsequent wire bonding onto a chip expander for electronic measurements.

First, the FET architecture influences the substrate selection with the need for an isolated gate electrode. Standard silicon wafers with 285 nm layer of thermally-grown $SiO_2$ comprise the substrate and a solid-state global back gate is implemented by contacting the underlying silicon with the $SiO_2$ layer acting as electrical isolation. As a matter of fact, the thickness of the oxide layer is chosen specifically to induce optical contrast from interference with the graphene layer [76], which allows the use of optical microscopy as a fast and easy inspection tool during sensor fabrication.

Second, the design of the gold contact electrodes reflects several considerations for the transfer of the CVD-grown graphene and a need for wire bonding onto chip expanders for electronic measurements. The electrode/graphene interface is a bottom-electrode contact which has been proved to be more reliable with lower contact resistance compared to top-electrodes [77, 78]. Every chip includes three Hall bar positions in case there are tears in the graphene layer after transfer that would make one Hall bar impossible to use for measurement. Additionally, the electrodes are of two thicknesses to further limit the tearing of graphene during transfer by employing only a thin layer of gold (25 nm) around the Hall bar positions with connection to high electrodes (100 nm Au), which are necessary for the wire bonding of the chip. Besides the electrodes, every chip also contains a guard ring around the edge, which prevents current leakage outside of the guard.

Third, the graphene layer is patterned into a Hall bar shape with regard to the parameter standards set by ASTM [79] to ensure correct measurements of electronic properties. Moreover, the graphene Hall bar can be covered by a polymer passivation layer, although this requires an additional lithographic step, because the bonding pads need to remain uncovered for wire bonding. The choice of a suitable polymer is critical as well due to the intended measurements at temperatures up to 200 °C, which is above the melting point of most commonly used resists (for example PMMA).

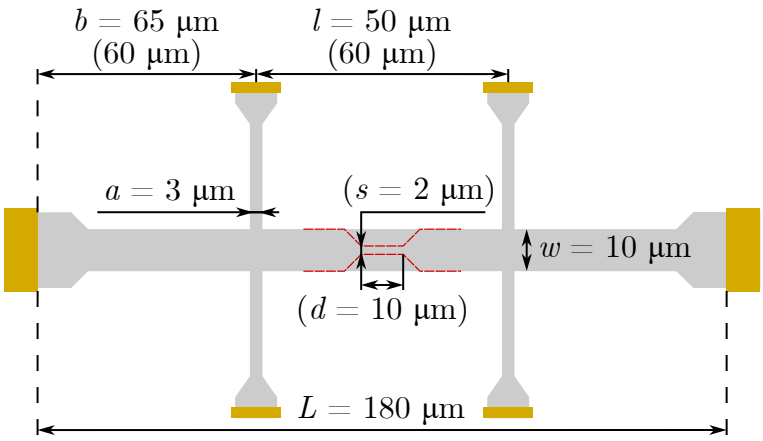


**Fig. 3.2:** Dimensions of the graphene Hall bar. The determining parameter is the width of the main channel $w$ with all other dimensions chosen to comply with the ASTM standards [79]. The gold ends of the graphene channels indicate contact to the pre-patterned electrodes on the substrate. The red dashed lines denote the optimized design with a constriction of the main channel. Dimensions in brackets correspond to the optimized design with the additional parameters (length $d$ and width $s$) of the constricted part.

Although the Hall bar shape might seem more complicated compared to the Hall cross, both patterns are equally demanding from a fabrication point of view and the Hall bar geometry actually presents multiple advantages for the planned electronic measurements. The aforementioned ASTM standards set lower and upper limits on the the length of the main channel $L$, the width of the side channels $a$ and the distance between the voltage and current contact $b$, based on the width of the main channel $w$: $L \geq 5w$, $w \geq 3a$, $b \geq 2w$. Fig. 3.2 illustrates the main parameters of the Hall bar and shows the dimensions chosen in our design for the graphene Hall probe. As part of an effort to optimize the sensor, we also fabricate a graphene Hall bar with a constriction in the middle of the main channel,

which is depicted by the red dashed lines. This optimization adds two more parameters to the Hall bar, length $d$ and width $s$ of the constricted part, which are written in brackets as well as the parameters $b$ and $l$ altered for the optimized version.

## 3.2 Graphene Hall probe fabrication

The fabrication of the graphene Hall probe uses standard, well-known methods and processes that are occasionally combined in a novel way to make the final procedure as simple, quick and reliable as possible. The main tool utilized throughout the whole process is lithography - a versatile method for the preparation of micro- to nanostructures by creating a pattern of choice in a polymer mask on top of the substrate.

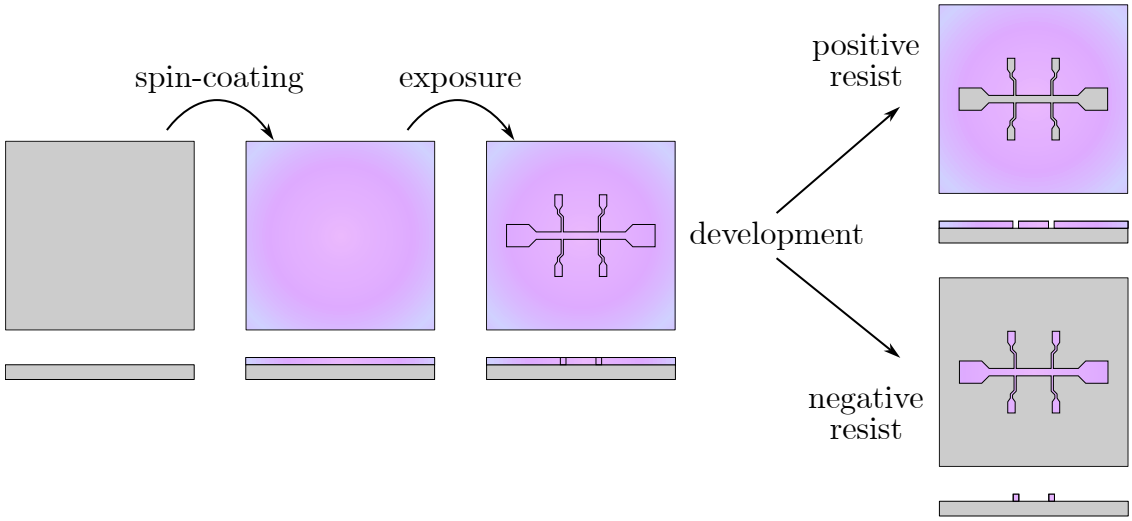


**Fig. 3.3:** Scheme of a standard lithography process showing both a top and side view of each step. First, a photoactive polymer (so-called resist) is spin-coated onto a clean substrate. Next, the resist undergoes structural changes upon exposure to either UV light or an electron beam. Finally, selective removal of specific areas of the resist during development results in the formation of the desired pattern. The developer removes the exposed regions for positive resists and vice versa for negative resists.

Fig. 3.3 illustrates a typical lithographic process. First, a thin layer of a photoactive polymer called resist is spin-coated on the substrate and baked on a hotplate for a short period of time to dry out. Next, the desired pattern is exposed into the resist layer either by UV light or a beam of electrons, which interacts with the chemical composition of the polymer. Afterwards, the sample is put into a developer, which etches the resist to create the exposed pattern. In general, resists are divided into positive and negative ones depending on their reaction to exposure, which weakens (strengthens) the structure of positive (negative) resists. Development then removes the exposed parts of positive resists and the non-exposed areas of negative resists. Although the exact parameters of the whole lithographic process depend mainly on the used resist, the choice of substrate can also influence the process conditions.

Overall, the fabrication procedure of the graphene Hall probes contains three pivotal parts, which are crucial for the functionality of the device: preparation of electrodes on the substrate, graphene transfer, and patterning of the graphene layer.

### 3.2.1 Patterning of electrodes

As a result of the design of the gold electrodes with two different thicknesses, the patterning of the substrate must be done in two separate lithographic steps, Fig. 3.4. To make this part of the fabrication process as easy and fast as possible, we have fabricated a lithographic mask containing patterns for both steps. This allows us to expose the whole pattern at once onto multiple chips using mask lithography (in contrast to direct writing systems which draw the pattern line by line).

First of all, the silicon wafer is lightly pre-cut by laser to 7 mm × 7 mm chips and broken up into pieces containing up to 6 × 6 chips each for the electrode patterning. Before any lithographic process, the substrate is cleaned in organic solvents (acetone, isopropyl alcohol) and in oxygen plasma for several minutes to minimize contamination and improve the adhesive properties of the surface. Next, the adhesion promoter AR 300-80 [80] and the positive optical resist AZ 701 MiR [81] are spin-coated onto the substrate. After exposure and development, the substrate is briefly subject to *reactive-ion etching* (RIE) by oxygen plasma to smooth out the edges of the exposed pattern in the resist. The deposition then consists of evaporating a thin adhesive layer of titanium (5 nm) and a layer of gold (25 nm in the first step) by electron beam physical vapour deposition. Finally, a standard lift-off process is used to remove the non-exposed resist, which leaves only the gold pattern on the substrate. This procedure is subsequently repeated for the second lithographic step with a deposition of 5 nm Ti / 100 nm Au, which completes the preparation of the electrodes on the substrate.

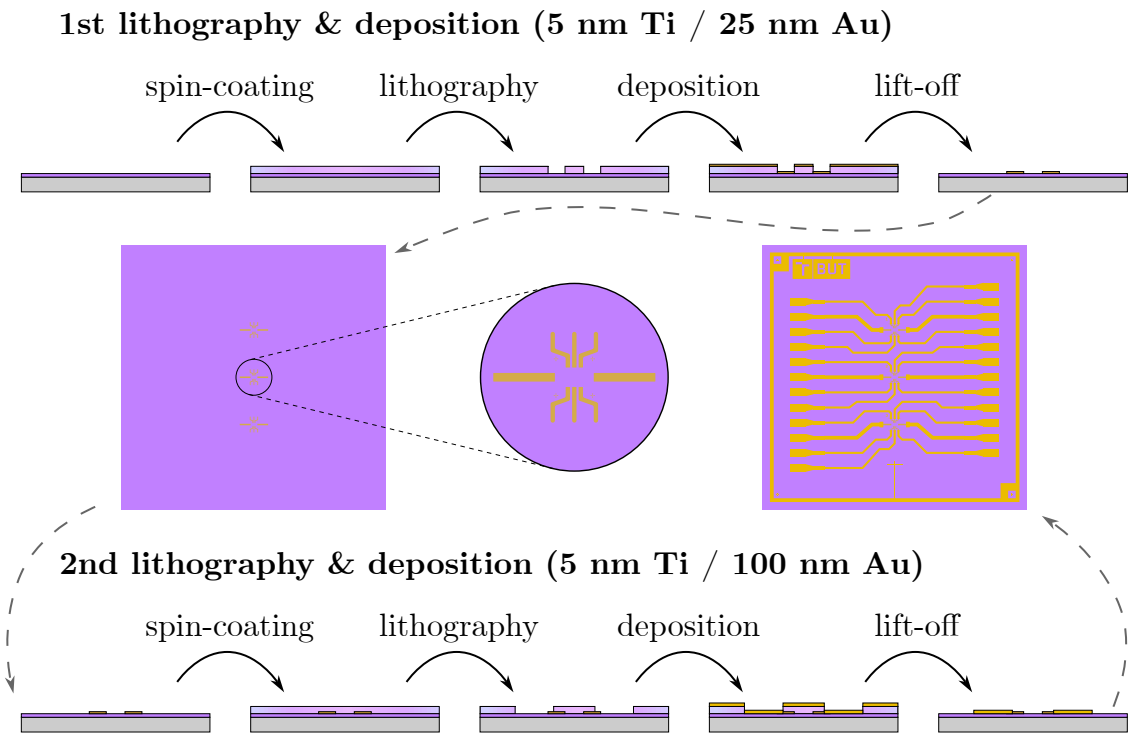


**Fig. 3.4:** The two-step fabrication procedure for the gold electrodes. Initially, positive UV lithography is performed on a clean substrate. Then, a 5 nm Ti / 25 nm Au layer is deposited and removed by lift-off to create the structure shown in the left top-side view. This process is repeated for the deposition of 5 nm Ti / 100 nm Au, resulting in the final electrode pattern shown in the right top-side view.

### 3.2.2 Graphene transfer

The next part concerns the transfer of the CVD-grown graphene onto prepared chips by the PMMA-assisted wet transfer method [82]. The pre-patterned pieces of wafer are broken up into individual chips, cleaned by organic solvents and oxygen plasma. The chips are then baked at 180 °C for at least 45 minutes to remove water from the $SiO_2$ layer, in preparation for transfer.

Fig. 3.5 illustrates the transfer procedure. Chemical vapour deposition grows graphene on both sides of the copper foil (Fig. 3.5a), therefore the first steps consist of spin-coating a PMMA layer on the top side (Fig. 3.5b) and then cleaning graphene from the bottom side of the copper foil by RIE with oxygen plasma (Fig. 3.5c). The PMMA layer serves two purposes here: protection of the top graphene during plasma cleaning and providing a support structure during the transfer from the copper foil onto the substrate. A double-layer of PMMA can be used to reduce the amount of residues left on the graphene layer. A thin bottom layer with shorter polymer chains (e. g. PMMA 50K) enables a cleaner removal and a thick top layer (e. g. PMMA 950K) acts as a scaffolding for graphene. The copper foil is fully etched away in $Fe(NO_3)_3 \cdot 9\,H_2O$ (Fig. 3.5d), which leaves the graphene/PMMA floating on the surface of the solution. The graphene/PMMA stack can be moved to different liquid solutions by carefully scooping it onto a clean chip. In this way, the graphene sample is cleaned of metallic residues in deionized water, hydrochloric acid (Fig. 3.5e) and again in deionized water. The graphene/PMMA is then placed directly onto the pre-patterned electrodes on the prepared chips (Fig. 3.5f). After drying out, the chip is covered by a droplet of liquid PMMA (Fig. 3.5g) to partially dissolve the supportive PMMA layer, which allows the graphene layer to relax and straighten on the substrate without forming tears. Finally, the remaining PMMA is removed in acetone (Fig. 3.5h) and the chip with graphene is baked at 180 °C for 15 minutes to improve adhesion of the graphene layer to the substrate.

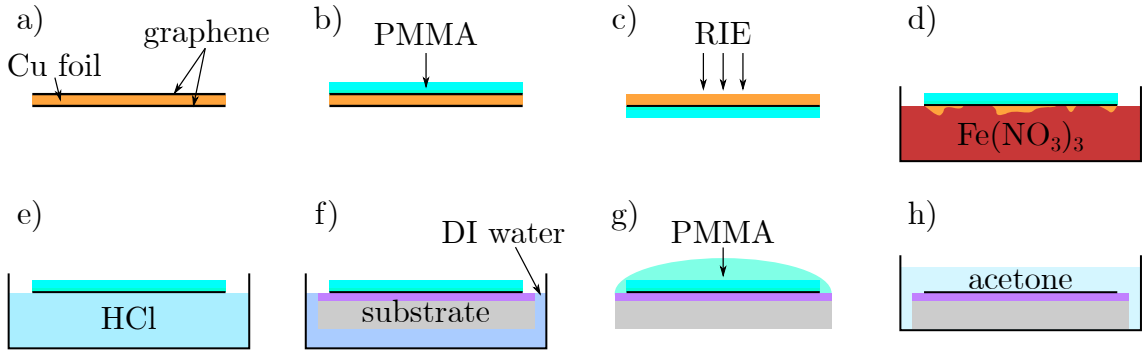


**Fig. 3.5:** The PMMA-assisted wet transfer process. a) CVD graphene is grown on both sides of the copper foil. b) A support layer of PMMA is spin-coated on the top layer of graphene. c) Graphene on the bottom side of the foil is removed by RIE in oxygen plasma. d) The copper foil dissolves in $Fe(NO_3)_3 \cdot 9\,H_2O$ and graphene with PMMA remains floating on the surface of the liquid. e) HCl is used to remove metallic contaminants from the copper foil and $Fe(NO_3)_3 \cdot 9\,H_2O$. f) The graphene/PMMA stack is scooped up from deionized water onto a prepared substrate and left to dry out. g) A droplet of liquid PMMA is applied to dissolve the support layer of PMMA. h) Finally, all remains of PMMA are removed in acetone.

### 3.2.3 Patterning of graphene

The most critical part in the fabrication of the graphene Hall probe is the patterning of the graphene layer into the Hall bar structure, which is also the step with the highest probability of failure. Graphene is a unique substrate for lithography, characterized by its specific adhesive properties and constraints on process conditions. For example, sonication is commonly used during lithographic processes, but in this case it would shake the graphene layer completely off the substrate. On the other hand, resists show excellent adhesion to graphene and from experience it is impossible to fully clean graphene of optical resists after lithography, which makes *electron beam lithography* (EBL) the most suitable method for lithography on graphene.

In practice, patterning of graphene involves more than just lithography, as the unwanted areas of the graphene layer must be removed by etching in oxygen plasma through a resist mask. In the literature, two types of resist are generally used for the patterning of graphene: PMMA and HSQ [68]. PMMA is a positive resist that leaves a minimal amount of residues on graphene. However, the fast etch rate of PMMA in oxygen plasma is a major drawback, limiting the exposure time of the graphene layer to plasma before the resist mask is etched through. In contrast, HSQ is a negative resist that is highly resistant to plasma etching due to its solidification into an amorphous $SiO_2$ layer during development. This fact also demonstrates its main problem: the final removal of the resist from the patterned graphene. One approach to address this challenge is to use a PMMA/HSQ multilayer, which combines the high plasma resistance of HSQ and simple removal of PMMA. Despite these advantages, potential issues may still arise in this process. Primarily, there is a risk of the HSQ on top sticking back to the sample as the PMMA underneath dissolves.

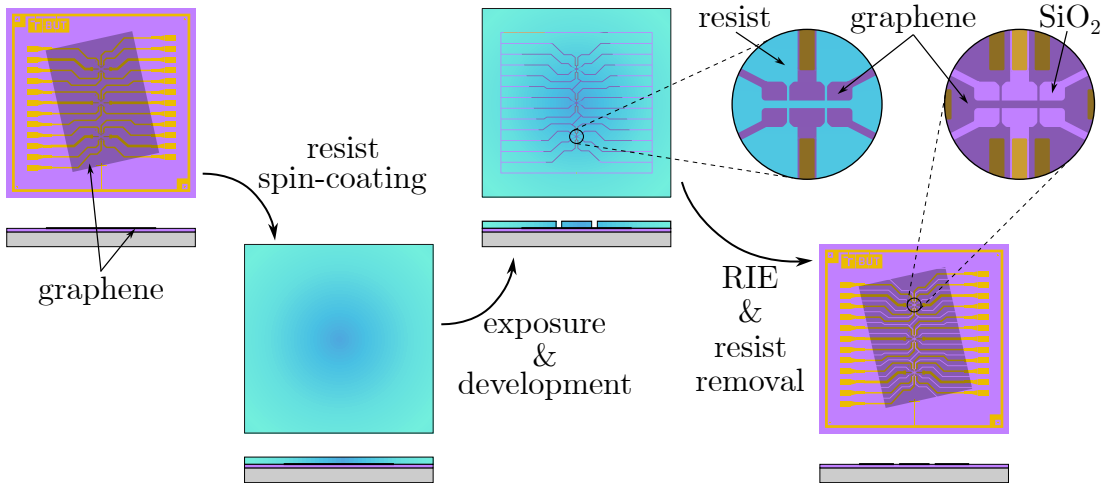


**Fig. 3.6:** The graphene patterning procedure with a positive EBL resist. A pre-patterned substrate with a transferred graphene layer is spin-coated with the resist. The exposure consists of two parts: array of lines to prevent short-circuitng of the gold electrodes and a rectangle with inverse Hall bar pattern (shown in the left detail). After development, the exposed parts of graphene are removed in oxygen plasma by RIE with the final Hall bar structure shown in the detail on the right.

Based on previous experience with PMMA and HSQ in our group, we have chosen to optimize a patterning procedure with a positive EBL resist called CSAR [83]. This resist is very similar to PMMA in many regards, however, CSAR offers better resolution and

twice as slow etch rate in oxygen plasma compared to PMMA, while retaining the same ease of removal from graphene.

The graphene patterning process with CSAR is depicted in Fig. 3.6. In preparation for lithography, the pre-patterned substrate with transferred graphene is cleaned in organic solvents and baked at 180 °C for 15 minutes before spin-coating of the adhesion promoter AR 300-80 and the CSAR resist. The exposure consists of two parts: a rectangular area containing the Hall bar design and an array of lines spanning the whole sample. The Hall bar pattern is in inverse due to the use a positive resist and the purpose of the lines is to prevent short-circuiting of the gold electrodes by severing the graphene layer between them. After development, the exposed graphene is etched in oxygen plasma and the remaining resist is removed in dioxolane.

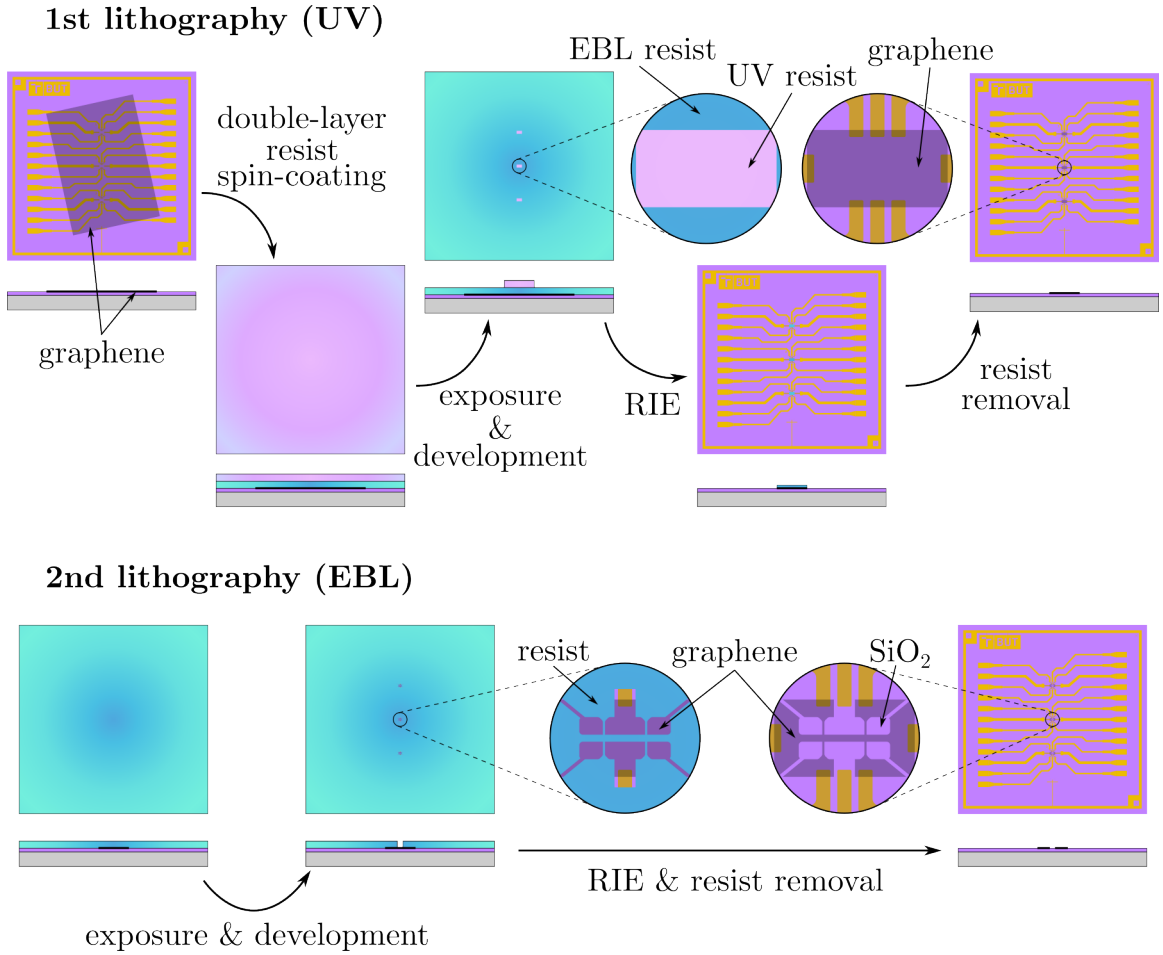


**Fig. 3.7:** The extended patterning procedure with two lithographic steps for graphene with tears or rolled-up edges. For the first lithography, a resist double-layer is spin-coated onto a pre-patterned substrate with transferred graphene. The top optical resist is exposed by UV light and both resists are etched in oxygen plasma, which also removes the rolled-up graphene edges. The sample is spin-coated again for the second lithographic step, which patterns the remaining graphene into the Hall bar structure.

Unfortunately, this process works correctly only if the graphene layer is transferred successfully without any large tears or rolled-up edges that are a common occurrence. A longer etching time is then necessary to remove these features. Although the adoption

of CSAR extends the possible exposure time to oxygen plasma, the rolled-up edges can still persist and short-circuit the gold electrodes. In order to solve this issue, we have introduced an additional lithographic step to the graphene patterning process, which further prolongs the etching time. Fig. 3.7 shows the extended version of the patterning procedure.

The added step is performed using optical lithography with a double-layer resist mask. For easy removal from graphene, CSAR or PMMA serve as the bottom resist with an optical resist on top with slower plasma etch rate. Despite the fact that the bottom EBL resist is not sensitive to UV light and is not developed, the oxygen plasma manages to etch through the bottom resist and reach the graphene layer before the top resist is fully removed. By incorporating this additional step, the possible plasma etching time of graphene can be multiplied by a factor of 2–3, depending on the combination of the top and bottom resists (we test this process with the combination of CSAR as the bottom resist and the optical resist AZ 701 MiR on top). For the selection of the resist double-layer, it is crucial to choose resists with different thinners. Otherwise, the bottom and top resist partially mix during spin-coating, which irregularly alters the etch rate of the top resist.

Finally, after successfully patterning the transferred graphene into the Hall bar structure, the sample is glued by conductive silver paste onto a chip expander and wire bonded by aluminium wire in preparation for electronic measurements. Fig. 3.8 shows an image of a pre-patterned chip with the fabricated graphene Hall probe and images captured by *scanning electron microscopy* (SEM) of the two Hall bar designs.

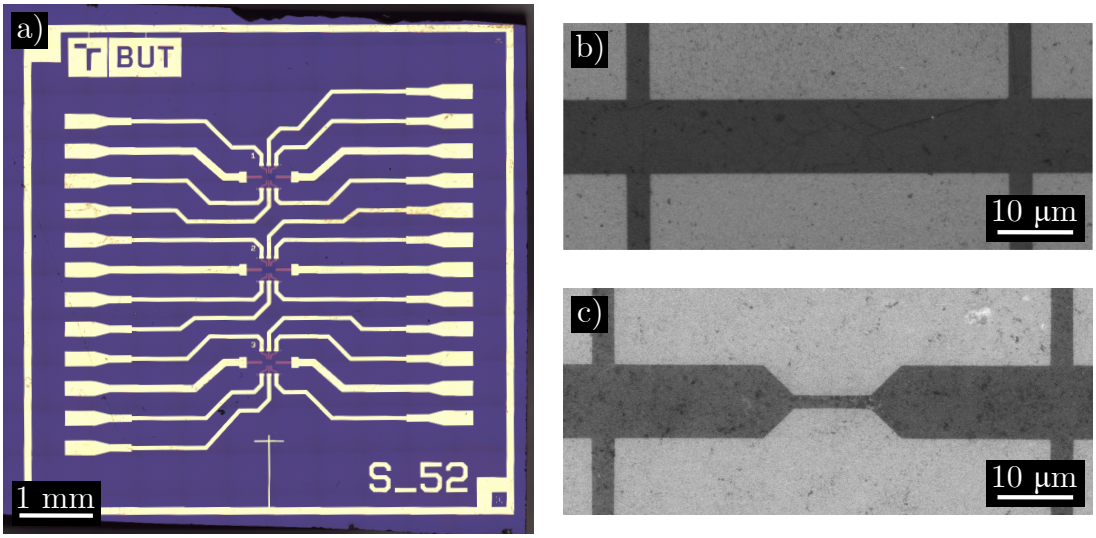


**Fig. 3.8:** Images of the fabricated graphene Hall probes. a) An overview of the pre-patterned substrate. b) SEM image of graphene patterned into a Hall bar with main channel width $w = 10\,\mu\text{m}$ and c) a graphene Hall bar with $2\,\mu\text{m}$ constriction in the middle of the $10\,\mu\text{m}$ main channel.

### 3.2.4 Passivation

As was already mentioned in the previous chapter (sec. 2.3), studies [48, 57, 63, 64, 69, 70] have demonstrated that incorporating a passivation layer on top of graphene enhances sensor performance. The testing of a passivation layer based on the SU-8 [84] resist is

another optimization of our graphene Hall probe, in addition to modifying the Hall bar pattern (sec. 3.1). SU-8 is a highly stable, heat-resistant optical resist, which has been chosen with consideration of the planned testing at temperatures up to 200 °C. However, the inclusion of the passivation layer requires an extra lithographic step, which covers the graphene layer with SU-8 and leaves the bonding pads exposed for wire-bonding of the graphene Hall probe onto a chip expander.

# 4 Characterization by Raman spectroscopy

Raman spectroscopy is a widely used technique for assessing the quality of graphene, given its ability to provide rapid and non-destructive analysis. This method offers valuable insights into the electronic structure of graphene and presence of defects in its lattice. To correctly interpret the Raman spectra of graphene, it is worthwhile to consider phonon dispersion in graphene. As a result of the unit cell containing two carbon atoms (sec. 1.1), the phonon dispersion relation consists of six branches, which can be classified into two in-plane optical (iTO and LO), two in-plane acoustic (iTA and LA), one out-of-plane optical (oTO) and one out-of-plane acoustic (oTA) phonon modes, Fig. 4.1a. The interaction of these phonon modes at the K and K' points gives rise to the characteristic peaks in the Raman spectra of graphene, Fig. 4.1b.

The most prominent features of the Raman spectrum are the G and 2D peaks appearing at $\sim 1585\,\mathrm{cm}^{-1}$ and at $\sim 2700\,\mathrm{cm}^{-1}$, respectively. Additionally, a third peak can appear at $\sim 1350\,\mathrm{cm}^{-1}$, referred to as the D peak as it is induced by disorders in the graphene lattice. The 2D peak derives its name from its frequency being approximately twice the D peak frequency, $\omega_{2D} \sim 2\omega_D$, however, it is not indicative of any presence of defects. Other weaker features can appear at $\sim 1620\,\mathrm{cm}^{-1}$ (so-called D' peak, which can be seen in the slightly asymmetric widening of the G peak to the right in Fig. 4.1b) and at $\sim 2450\,\mathrm{cm}^{-1}$ (the G$^*$ peak in Fig. 4.1b).

There are two main scattering processes that are responsible for the electron-phonon interactions in graphene: first-order and double resonance. The G peak is a first-order Raman resonance (Fig. 4.2a), in which an electron absorbs an incoming photon, scatters on a phonon and emits a photon upon recombining with a hole. The G peak is associated with the doubly degenerate iTo and LO branches at the Γ point (Fig. 4.1a), which corresponds to the in-plane vibration of the $sp^2$ carbon bonds [86].

Both the D and 2D peaks arise from the double resonance Raman scattering mechanism, Fig. 4.2b and c. In this process, an electron around the $K$ point absorbs a photon,

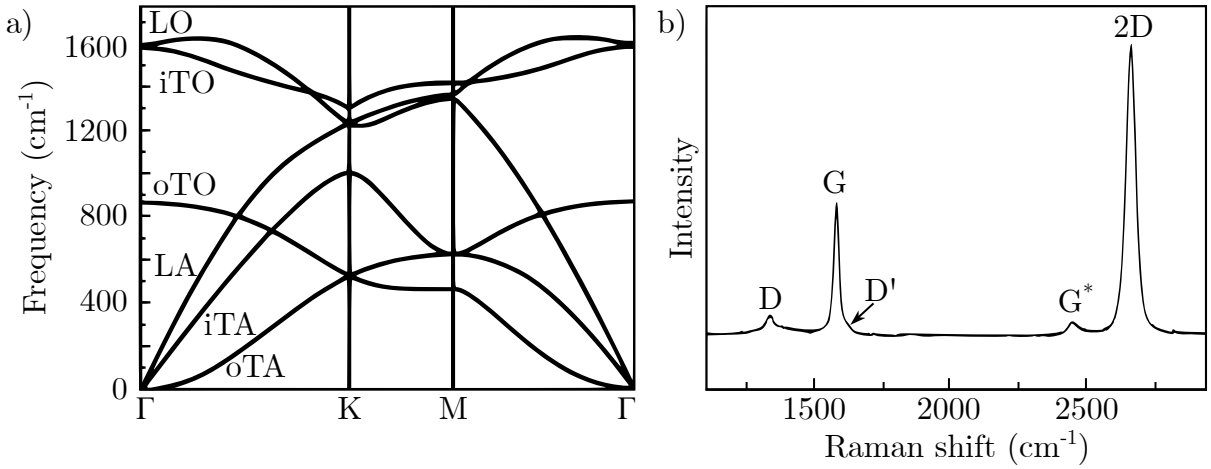


**Fig. 4.1:** a) Calculated phonon dispersion relation of graphene showing the six phonon branches along the main directions in the first Brillouin zone, adapted from [85]. b) A representative Raman spectrum of our graphene samples. Most prominent are the G and 2D peaks, which are characteristic of graphene. The spectrum also exhibits weaker features such as the D, D' (partially obscured by the G peak) and G$^*$ peaks.

which is followed by the scattering of the electron by a phonon or a defect towards the *K'* point. Subsequently, the electron is scattered back to the *K* point by a phonon, where it recombines with a hole, resulting in photon emission. For the D peak, the first scattering event is elastic involving a crystal defect, which is needed to activate it [87]. In the case of the 2D peak, two iTO phonons cause inelastic scattering of the electron between the

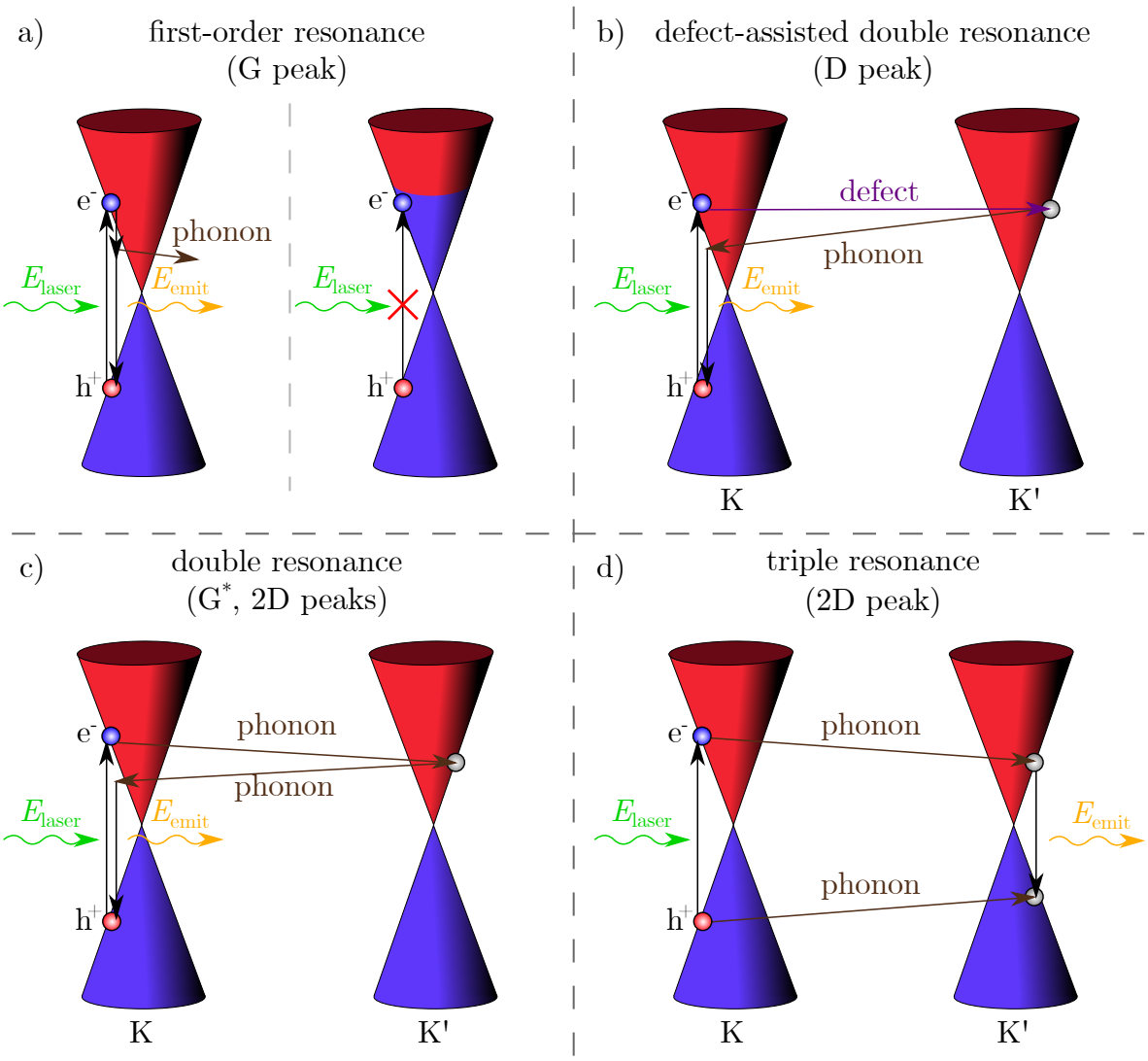


**Fig. 4.2:** The main electron-phonon scattering processes in graphene, which are responsible for the individual peaks in the Raman spectrum. a) First-order resonance: a photon with energy $E_{\text{laser}}$ is absorbed by an electron, which then recombines with a hole emitting a phonon and a photon with energy $E_{\text{emit}}$ (left). The initial intraband transition is forbidden by Pauli exclusion principle due to doping (right). b) and c) Double resonance: incoming photon creates an electron-hole pair around the *K* point, the electron is then scattered to the *K'* point and back. One of the scattering events is always enabled by a phonon, the other scattering event can be elastic on a lattice defect (b) or inelastic involving another phonon (c). d) Triple resonance: incoming photon creates an electron and a hole around the *K* point, these are scattered by identical phonons with opposite wave vectors to the *K'* point, where the electron-hole pair recombines emitting a photon.

$K$ and $K'$ points. A suitable combination of phonons with different wave vectors can also enable double resonance, which manisfests as weaker features in the spectrum [88]. For example, the G$^*$ peak in our spectrum in Fig. 4.1b originates from a double resonance scattering process involving one iTO phonon and one LA phonon near the $K$ point.

Additionally, a triple resonance can arise in graphene samples of high quality, Fig. 4.2d. In this case, a photon induces the generation of an electron-hole pair around the $K$ point. However, both the electron and the hole are scattered to the $K'$ point by identical phonons with opposite wave vectors. Following this, the electron-hole pair recombines at the $K'$ point, leading to the emission of a photon. Contrary to the double resonance, triple resonance requires that all the intermediate states are in resonance as well as the final and initial states, e.g. all states lie on the surface of the Dirac cones representing the valence and conduction bands (resonant states are illustrated as filled circles in Fig. 4.2). To fulfill this condition, the valence and conduction bands need to be mirroring each other with respect to the Fermi level, e.g. the dispersion relation must be linear with little to no doping. Malard et al. suggested that this triple resonance process may contribute to the high intensity of the 2D peak compared to the intensity of the G peak in the Raman spectra of monolayer graphene [85].

To summarize, the quality of graphene samples can be judged by several features in the Raman spectrum. The presence and intensity of the D peak is the most reliable indicator as defects are needed to enable double resonance for these phonon modes. Next, the position and shape of the 2D peak can be used to determine the number of graphene layers [89] with a single Lorentzian peak at $\sim 2680\,\mathrm{cm}^{-1}$ indicating a monolayer. Another commonly used metric to estimate the number of layers is the ratio of intensities of the 2D and G peaks, $I(\mathrm{2D})/I(\mathrm{G})$, however, both of these peaks show a clear dependence on doping of the graphene layer [90]. Multiple factors, including graphene origin and processing history, need to be taken into consideration when evaluating Raman spectra of graphene.

## 4.1 Influence of fabrication on graphene quality

Processing of graphene is a necessary step in fabricating graphene Hall probes due to the need for a defined shape of the graphene layer. As a consequence of the 2D nature of graphene, fabrication procedures frequently cause contamination of the graphene layer that is either irreversible or highly challenging to undo [91]. In fact, the most common type of contamination from processing are polymer residues, which can arise both from the transfer procedure or during subsequent lithographic steps. Raman spectroscopy can remarkably well reveal the presence of charged impurities or contaminants as they can both induce defects in the graphene lattice and cause doping of the graphene layer [92]. Here, we utilize this technique as an inspection tool to evaluate the influence of individual fabrication steps described in sec. 3.2 on the quality of the graphene layer in our devices.

First, we asses the variety in graphene samples after transfer onto the pre-patterned chips. As preparation for the Raman spectroscopy measurements, all samples are left in acetone heated to 50 °C for at least half an hour in order to chemically remove as much PMMA residue as possible. Afterwards, the samples are baked at 180 °C for 15 minutes to remove molecules adsorbed on top of graphene. Because single Raman spectra provide information only about a small area of graphene (about the spot size of the laser, which is in the order of units of µm), we perform Raman mapping with single spectra taken at points in 1 µm intervals over graphene area of 100 µm × 50 µm.

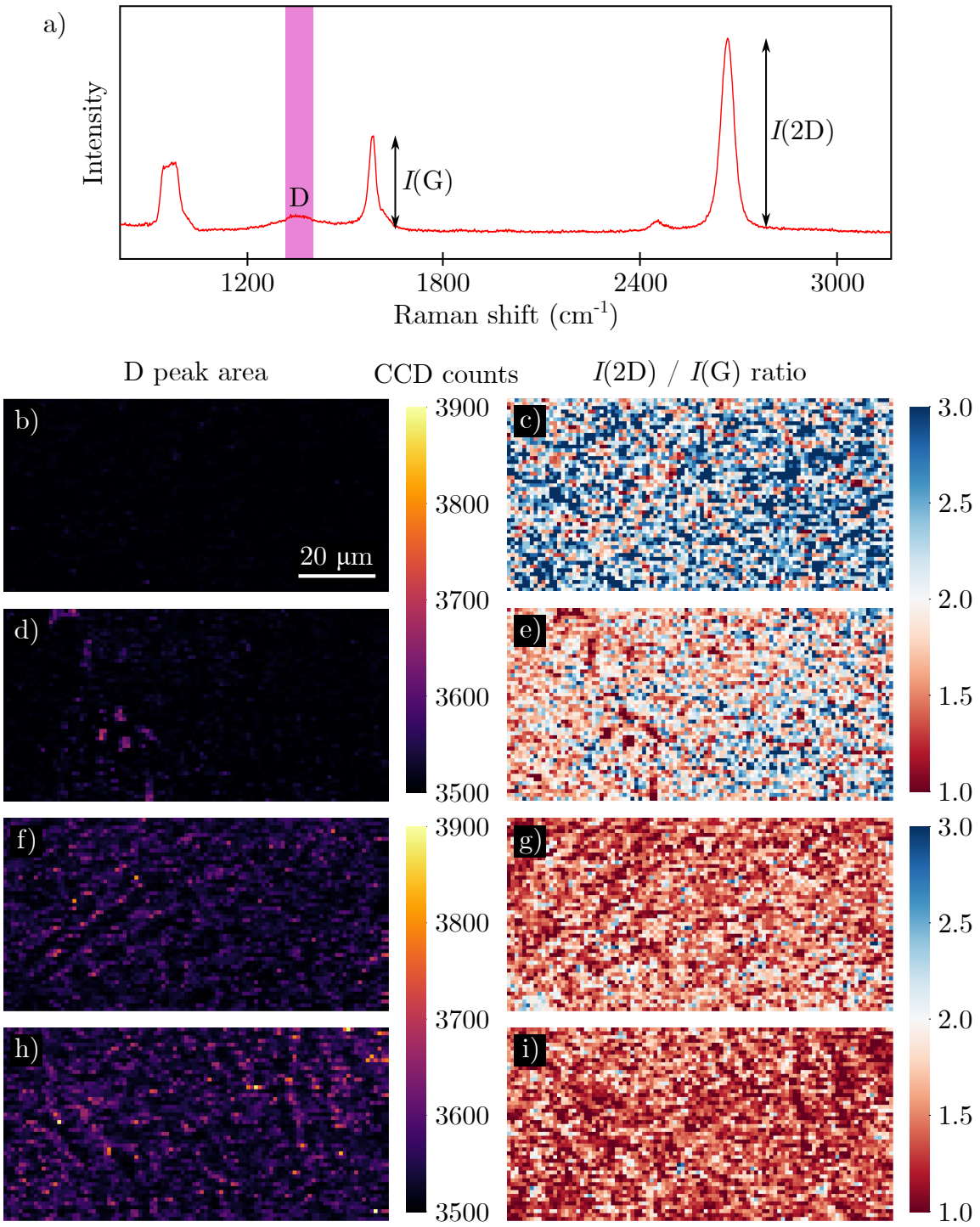


**Fig. 4.3:** Variety in the quality of graphene samples after transfer. a) A representative Raman spectrum of one of our graphene samples after transfer. Highlighted is the part of the spectrum around the D peak, used for calculating the D peak area in the left set of maps, and the intensities of the G and 2D peaks, used for calculating the $I(2D)/I(G)$ ratio in the right set of maps. For the D peak maps, the lower colour bar limit of 3 500 CCD counts corresponds to the level of background noise, e. g. no presence of D peak. For the $I(2D)/I(G)$ maps, a ratio of two and higher is indicative of high quality graphene with little to no doping. All maps b)-i) show graphene area of 100 µm × 50 µm with Raman spectra measured at points in 1 µm intervals. Each pair of maps, b) and c), d) and e), f) and g), h) and i), corresponds to a different graphene sample.

As previously mentioned, the main features in the Raman spectra for estimating graphene quality are the presence of the D peak, the shape of the 2D peak corresponding to the number of graphene layers, and the ratio of intensities of the G and 2D peaks $I(2D)/I(G)$. Based on the measured spectra of our graphene samples, we create maps tracking two of these features: the D peak and the $I(2D)/I(G)$ ratio. Fig. 4.3a shows a representative Raman spectrum of our graphene with highlighted area of the D peak and marked intensities of the G and 2D peaks, $I(G)$ and $I(2D)$, respectively. For the left set of maps in Fig. 4.3, we sum the measured CCD counts of the highlighted part of the spectrum to check for the presence of the D peak at every point of the Raman map. The lower limit of the colour bar (3 500 CCD counts) corresponds to summing over background noise and the upper limit (3 900 CCD counts) gives D peak intensity $I(D) \approx I(G)/5$. For the right set of maps in Fig. 4.3, we calculate the $I(2D)/I(G)$ ratio at every point of the Raman map. As a rule of thumb, a ratio of 2 or higher is considered desirable in the literature, hence the colour bar is centered around this value. A low $I(2D)/I(G)$ ratio can be caused by doping of the graphene layer. Intensities of both peaks diminish as doping increases, as certain transitions are prohibited by the Pauli exclusion principle (Fig. 4.2a). The decrease in the intensity of the 2D peak occurs more rapidly compared to that of the G peak. Although the initial excitation of electrons may be permitted, the subsequent scattering on phonons in the double resonance mechanism could be hindered by the Pauli exclusion principle.

Fig. 4.3 presents the variation in graphene quality after transfer illustrated on four different graphene samples. All these graphene layers originate from a single piece of copper foil and are transferred simultaneously under identical conditions. Nevertheless, the outcomes vary from clean to heavily contaminated graphene layers, as is evident both in the D peak maps on the left and in the $I(2D)/I(G)$ ratio maps on the right. In particular, Fig. 4.3d and e effectively demonstrate the correlation between the presence of the D peak in small areas and a low $I(2D)/I(G)$ ratio in the same spots. Clearly, the PMMA-assisted wet transfer procedure can significantly impact the quality of the transferred graphene layers.

Next, we perform the same sets of Raman spectroscopy measurements after each lithographic step in the extended version of the graphene patterning process (sec. 3.2.3) and analyze the changes in graphene quality induced by each step. Again, the samples are cleaned in acetone heated to 50 °C for 30 minutes and baked at at 180 °C for 15 minutes before measurement. Additionally, we anneal the graphene Hall bar in $H_2$ atmosphere for 30 minutes at 400 °C to try and thermally decompose the polymer residues.

Fig. 4.4 demonstrates the influence of fabrication processes on graphene quality. We compare both single Raman spectra (Fig. 4.4a) and Raman mapping of the D peak and $I(2D)/I(G)$ ratio for a graphene sample after transfer (Fig. 4.4b and c), UV lithography (Fig. 4.4d and e), electron beam lithography (Fig. 4.4f and g) and annealing (Fig. 4.4h and i). The Raman spectra in Fig. 4.4a are normalized to the silicon peak of the substrate at $\sim 950\,\mathrm{cm}^{-1}$ and together with the corresponding maps show a clear degradation of the graphene layer. Each fabrication step induces more defects in the graphene lattice (supported by the increased presence of the D peak) and causes a reduction in the $I(2D)/I(G)$ ratio. While annealing appears to diminish the presence of defects (Fig. 4.4h), this can be attributed to the overall reduction in signal intensity in the graphene spectrum after annealing and single spectra still exhibit a relatively prominent D peak (Fig. 4.4a). Although the impact is most pronounced following the first lithography, it should be noted that the successive processes exacerbate these effects.

In order to reduce the number of processing steps affecting graphene, we try to opti-

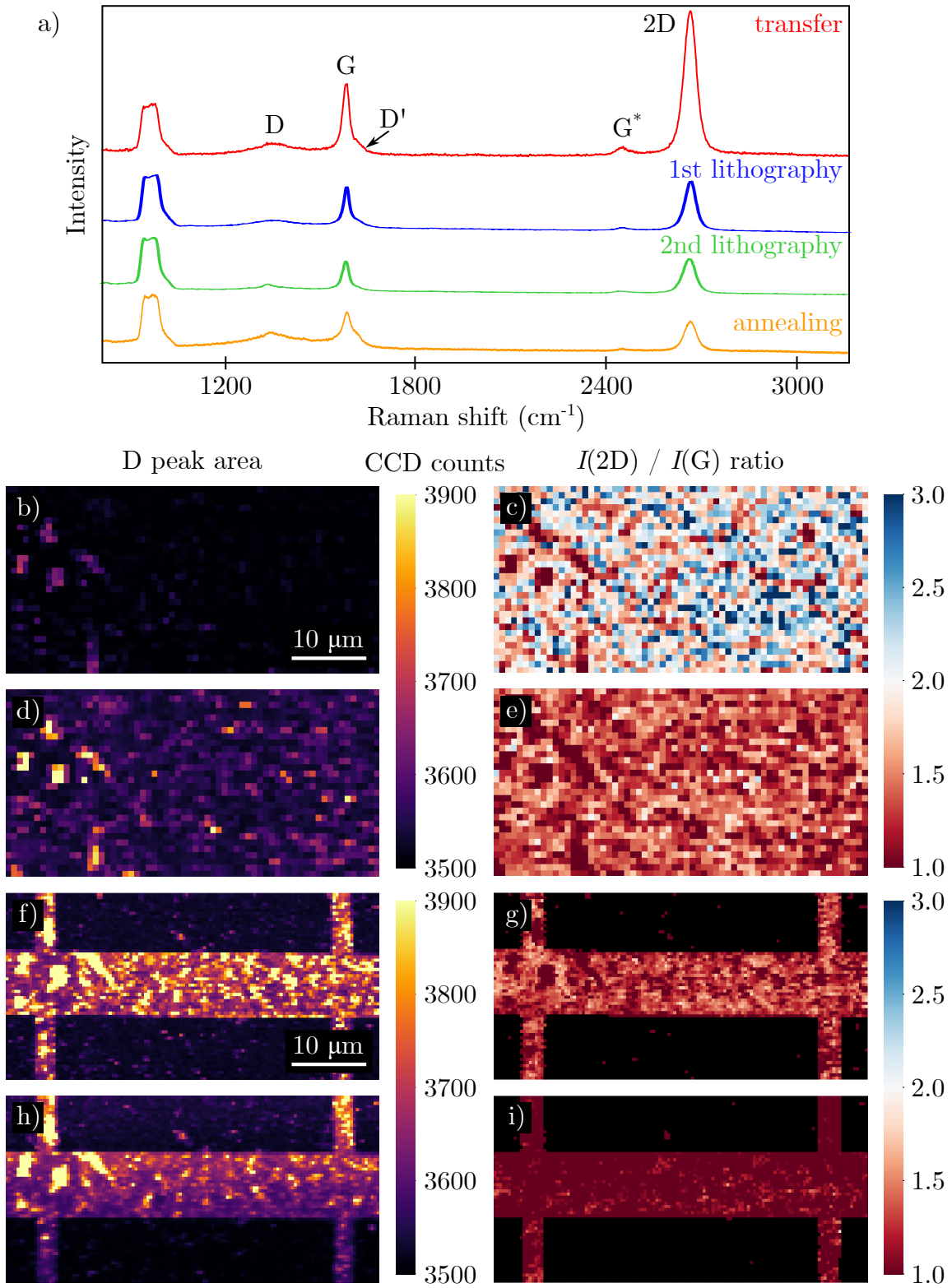


**Fig. 4.4:** Influence of fabrication on the quality of graphene. a) Representative Raman spectra after each processing step with corresponding mapping of the sample, b) and c) after graphene transfer, d) and e) after UV lithography, f) and g) after EBL, h) and i) after annealing at 400 °C in $H_2$ atmosphere for 30 min. All maps are created in the same manner as in Fig. 4.3 and show an area of 60 µm × 30 µm. Raman spectra in maps b)-e) are measured at points in 1 µm intervals and in maps f)-i) at points in 0.5 µm intervals.

mize the fabrication procedure for the constricted graphene Hall bars. Even though the patterning of graphene involves two separate lithographic steps, we opt to forgo removing the remains of the EBL resist following UV lithography and RIE in oxygen plasma and instead spin-coat a fresh layer of CSAR straight on top of the remains. In this case, the graphene layer directly experiences only one instance of spin-coating and resist removal. Fig. 4.5 presents the results of this optimized procedure. Unfortunately, the initial poor quality of the transferred graphene renders it impossible to confirm or refute any improvements that can be attributed to this modification.

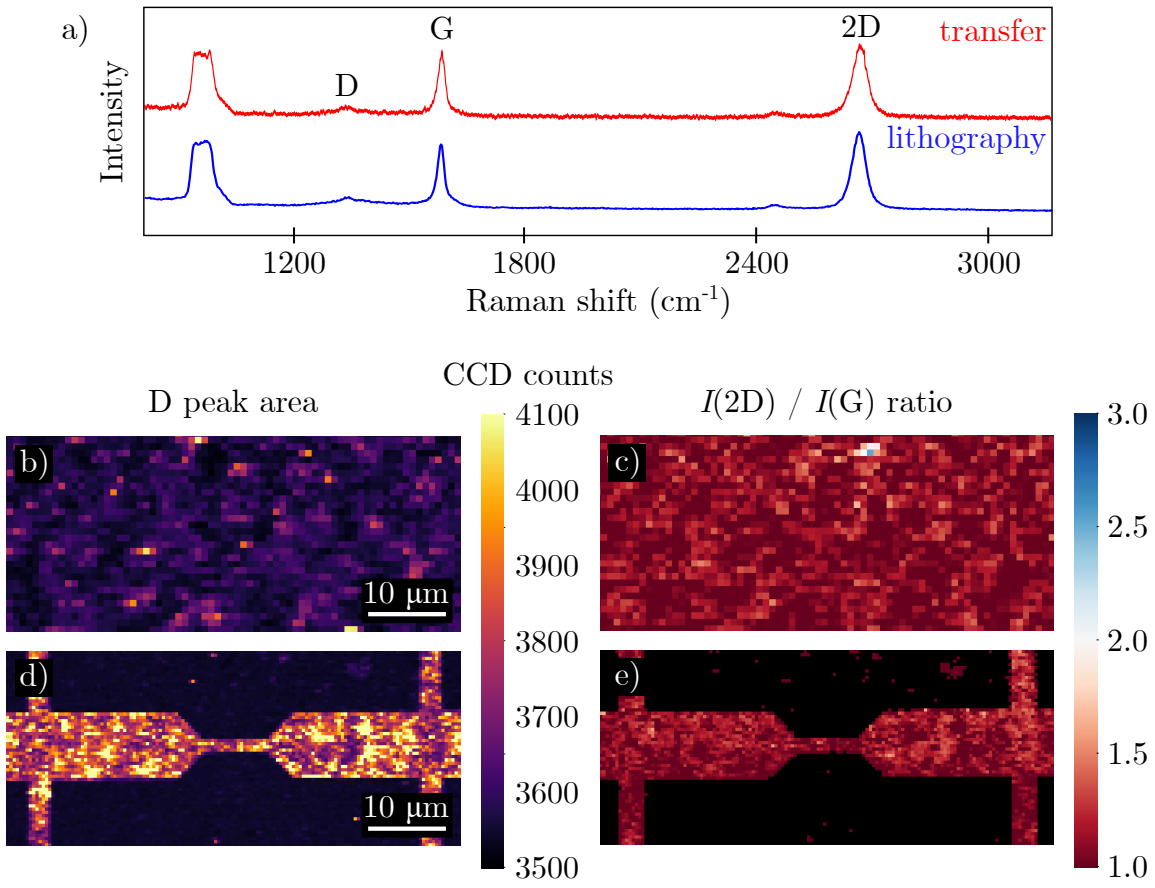


**Fig. 4.5:** Effect of the optimized fabrication procedure on the quality of graphene. a) Representative Raman spectra after each processing step with corresponding mapping of the sample, b) and c) after graphene transfer, d) and e) after patterning of graphene into a constricted Hall bar. All maps are created in the same manner as in Fig. 4.3 and show an area of 70 µm × 30 µm. Raman spectra in maps b) and c) are measured at points in 1 µm intervals and in maps d) and e) at points in 0.5 µm intervals.

The characterization of the fabricated graphene Hall bars by Raman spectroscopy reveals a substantial presence of defects and diminished intensities of the G and 2D peaks, possibly indicating doping in the graphene layer. Das et al. experimentally measured the charge carrier density for various values of the $I(2D)/I(G)$ ratio [90]. According to their data, $I(2D)/I(G) \approx 2$ corresponds to charge carrier concentration $n \approx 3 \cdot 10^{12}\,\mathrm{cm}^{-2}$. However, if we consider the parallel-plate capacitor model for our graphene FET (eq. 2.9) with a 285 nm $SiO_2$ isolation layer between an undoped graphene channel and a solid-state back gate, the application of gate voltage $V_G \approx 40\,\mathrm{V}$ would be necessary

to achieve doping equal to $n \approx 3 \cdot 10^{12}\,\mathrm{cm}^{-2}$. A ratio $I(2D)/I(G) \approx 1$ corresponds to charge carrier concentration $n \approx 2 \cdot 10^{13}\,\mathrm{cm}^{-2}$, which would necessitate application of gate voltage $V_G \approx 270\,\mathrm{V}$. Considering that all graphene Hall bars exhibit $I(2D)/I(G) \approx 1$–$1.5$ after fabrication, we should not be able to detect the Dirac point within the range of our transport measurements ($V_G = \pm 80\,\mathrm{V}$). However, this is not the case. At room temperature, our graphene Hall probes show Dirac point voltage $V_D \approx 35\,\mathrm{V}$. This implies that during the Raman spectroscopy measurements conducted without the application of a gate voltage, the graphene layer should have a charge carrier density $n \approx 2 \cdot 10^{13}\,\mathrm{cm}^{-2}$ and the corresponding Raman map should appear as white-to-blue. While this inconsistency warrants further study, this falls outside the scope of this work.

# 5 Testing of the graphene Hall probes

There are two primary characteristics of our graphene Hall probes that we aim to test: their response to magnetic fields and their behaviour with increasing temperature. The first is a key prerequisite for any functional Hall probe, whereas the second is an area of research that has not been studied extensively in the literature. Additionally, we want to take advantage of the FET configuration to maximize the performance of the sensor.

## 5.1 Experimental setup

The transport and Hall effect measurements are conducted simultaneously in ambient conditions with the possibility of applying a magnetic field and heating as required. The experimental setup allows for a systematic evaluation of the interdependence between transport properties and the Hall effect in graphene by varying the following parameters: temperature, magnetic field strength, and carrier density.

For the application of a magnetic field, the expander with a wire bonded chip is positioned in the middle between a pair of ferrite magnets with an area of 5 cm × 5 cm. The large dimensions of the magnets ensure a uniform magnetic field across the entire sample. Moreover, the magnitude of the field can be adjusted by altering the distance between the pair of magnets. The strength of the magnetic field for a given separation between magnets is measured by the commercial gaussmeter GM08 from Hirst Magnetic Instruments Ltd. [93].

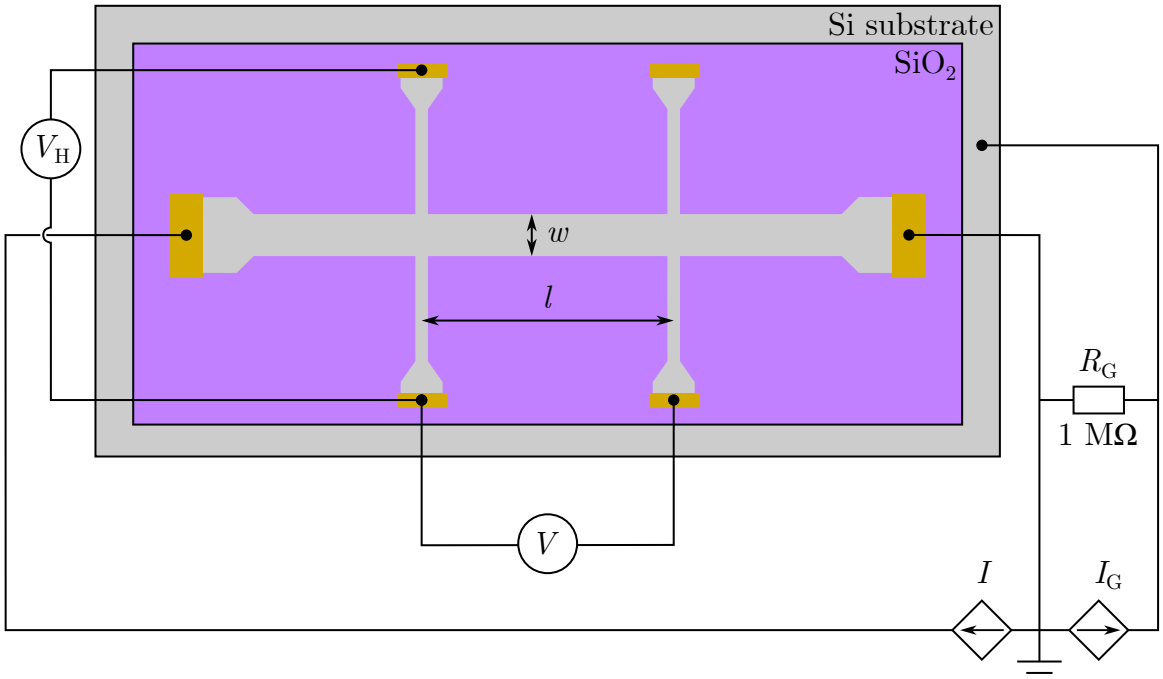


**Fig. 5.1:** Scheme of the electronic setup for the transport and Hall effect measurements. A current source supplies the main channel current $I$ and a pair of nanovoltmeters measures the longitudinal voltage $V$ and the transversal Hall voltage $V_H$ on the side channels. The back gate voltage $V_G$ between the graphene Hall bar and the silicon substrate is created by a gate current $I_G$ flowing through the gate resistor $R_G$.

To facilitate heating during measurements, the graphene Hall probe is secured onto a thin aluminium slab that features a heating element (a planar series resistor) on the other side. Inside the aluminium slab, a Pt100 temperature sensor is inserted and affixed with thermal paste to correctly measure the temperature. It is worth noting that the chip expander itself is also made of aluminium. The assumption is made that temperature distribution is relatively uniform across the various components of the heating system (the chip, the expander, the aluminium slab, and the heating element) due to the high thermal conductivity of metals. Consequently, the temperature measured by the Pt100 sensor is considered representative of the temperature of the graphene Hall probe.

The last part of the measurement setup concerns the electronic equipment, Fig. 5.1. A constant DC current $I$ is supplied to the main channel by a Keithley 6221 AC and DC Current Source. The longitudinal voltage $V$ and the transverse Hall voltage $V_{\mathrm{H}}$ are measured by a pair of Keithley 2182A Nanovoltmeters on the side channels of the graphene Hall bar. Another Keithley 6221 AC and DC Current Source is used for the application of gate voltage $V_{\mathrm{G}}$ between the silicon substrate and the graphene layer by running a gate current $I_{\mathrm{G}}$ through a gate resistor $R_{\mathrm{G}} = 1\,\mathrm{M\Omega}$.

By measuring the longitudinal voltage $V$, the sheet resistivity of the graphene layer $\rho_{\mathrm{s}}$ can be calculated as:

$$\rho_{\mathrm{s}} = \frac{w}{l}\frac{V}{I}, \tag{5.1}$$

where $w$ is the width of the main channel and $l$ is the distance between the side channels used for the measurement of the longitudinal voltage $V$ at constant current $I$. For the constricted Hall bar design, the sheet resistivity is calculated with an average of the main channel width $w_{\mathrm{c}} = 8.3\,\mu\mathrm{m}$.

The Hall bar geometry offers a considerable advantage in the measurement of transport properties of graphene. When using the same probes that are used for current supply at the ends of the main channel for measuring the longitudinal voltage (so-called two-probe measurement), the measured resistance includes the contribution of the metal contacts. However, by employing the four-probe measurement enabled by the Hall bar geometry, the resistance of the voltage contacts becomes irrelevant. This is attributed to the absence of current flow through the nanovoltmeter due to its large internal resistance. On the other hand, the Hall cross geometry necessitates the use of the more complex van der Pauw method to eliminate the contact resistance [16].

## 5.2 Results

The graphene Hall probes undergo testing in a temperature range spanning from room temperature up to 200 °C, both with and without a magnetic field whose magnitude and polarity are determined by the placement of the magnets. The measurement sequence is as follows: First, the magnets are positioned at a fixed distance if the magnetic field is applied. Then, the graphene Hall probe is gradually heated to 200 °C with individual measurements taken at 10 °C intervals. Afterwards, the sample is left to cool down before the next cycle of measurements in a different magnetic field. During each measurement, the gate voltage is swept from $0\,\mathrm{V} \rightarrow 80\,\mathrm{V} \rightarrow 0\,\mathrm{V}$ with $1\,\mathrm{V}/0.1\,\mathrm{s}$ step, while the temperature and magnetic field are held constant. The gate voltage range is chosen with respect to the initial p-doping of the graphene layer. Unless stated otherwise, the main channel current is set to $I = 1\,\mu\mathrm{A}$.

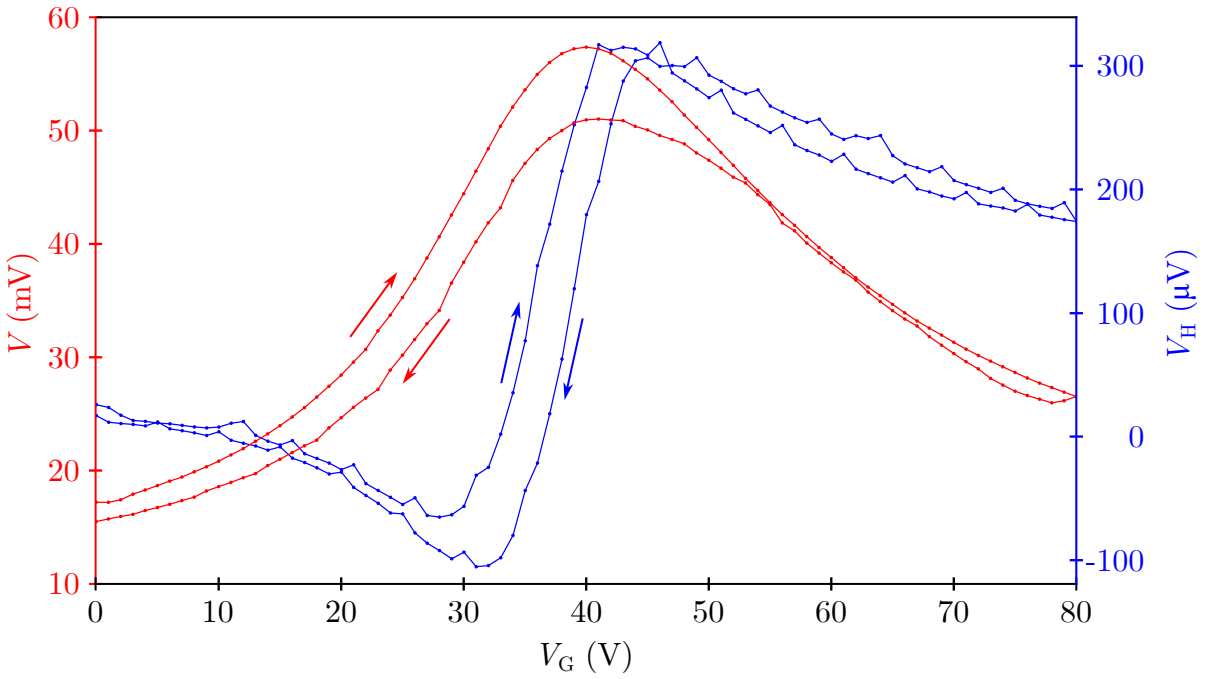


**Fig. 5.2:** Representative measurement of the graphene Hall probes in a magnetic field with the application of gate voltage. The longitudinal voltage $V$ indicates the doping of the graphene layer with the maximum of the curve corresponding to the Dirac point voltage $V_D \approx 40\,\mathrm{V}$. The Hall voltage $V_H$ shows the expected dependence on the charge carrier density $V_H \propto {n_{2D}}^{-1} \propto V_G^{-1}$ only far away from the Dirac point for both types of carriers, with a sharp reversal for $V_G = (30\text{–}40)\,\mathrm{V}$. All measurements exhibit hysteresis between forward and backward sweeps of the gate voltage $V_G$, which is evident both in the longitudinal voltage $V$ and Hall voltage $V_H$. The plotted data are measured on the constricted graphene Hall bar with SU-8 in a magnetic field $B = -183.6\,\mathrm{mT}$ at $T = 30\,^\circ\mathrm{C}$.

Fig. 5.2 presents a typical response of our graphene Hall probes in a magnetic field to the application of gate voltage $V_G$, both for the longitudinal voltage $V$ and the Hall voltage $V_H$. The longitudinal voltage $V$ represents the doping of the graphene layer with the peak of the curve at $V_G \approx 40\,\mathrm{V}$ corresponding to the crossing of the Fermi level through the Dirac point. In agreement with Eq. 2.7, the Hall voltage $V_H$ follows the $V_H \propto {n_{2D}}^{-1} \propto V_G^{-1}$ dependence for high charge carrier concentrations. Nonetheless, for low charge carrier concentrations, we observe the same abrupt reversal as reported in the literature. This behaviour close to the Dirac point has been attributed to the presence of a small energy overlap between the valence and conduction bands [1]:

$$\delta\varepsilon = n_0 \frac{\pi\hbar^2}{2m_e}, \tag{5.2}$$

where $n_0$ is a typical charge carrier density in the transition period, $\hbar$ is the reduced Planck constant and $m_e$ is the electron rest mass. We calculate the typical carrier density around the Dirac point from the Hall coefficient $n_0 = 1/(eR_H) = 8.26 \cdot 10^{11}\,\mathrm{cm}^{-2}$ to obtain an estimate for the energy overlap of our graphene samples $\delta\varepsilon \approx 1\,\mathrm{meV}$, which is in agreement with $\delta\varepsilon \approx 4\,\mathrm{meV}$ cited in [1].

Additionally, all of our measurements exhibit a noticeable hysteresis, which becomes apparent when comparing the forward and backward voltage sweeps. This hysteretic behaviour can be explained by the adsorption of water from air humidity on the surface of the graphene Hall bar [94]. However, also graphene Hall probes with the SU-8 passivation layer show some hysteresis, probably due to water molecules trapped between graphene and $SiO_2$. Although the samples are baked at 180 °C multiple times during the fabrication procedure, annealing in UHV conditions would be necessary to completely eliminate the trapped molecules. For the sake of clarity, the hysteresis behaviour is omitted in the following analysis and only data obtained from forward voltage sweeps are presented.

### 5.2.1 Reaction to magnetic field

A strong, consistent reaction to an external magnetic field is a fundamental property of any functional Hall probe. We measure the response of our graphene Hall probes in several magnetic fields of varying strength in both polarities and also without any applied magnetic field. Fig. 5.3 demonstrates that a stronger magnetic field $B$ elicits a larger Hall voltage response $V_H$. Switching the polarity of the applied field results in a corresponding change in the sign of the Hall voltage. It is noteworthy that our graphene Hall probes display a non-zero response even in the absence of any magnetic field ($B = 0\,\mathrm{mT}$), so-called offset Hall voltage. This offset voltage is commonly attributed in the literature to asymmetry in the geometry of the graphene Hall element. Additionally, the offset voltage is the reason why the Hall voltage response is not symmetrical, e.g. $V_H = 0\,\mu\mathrm{V}$ does not correspond to $V_G = V_D$.

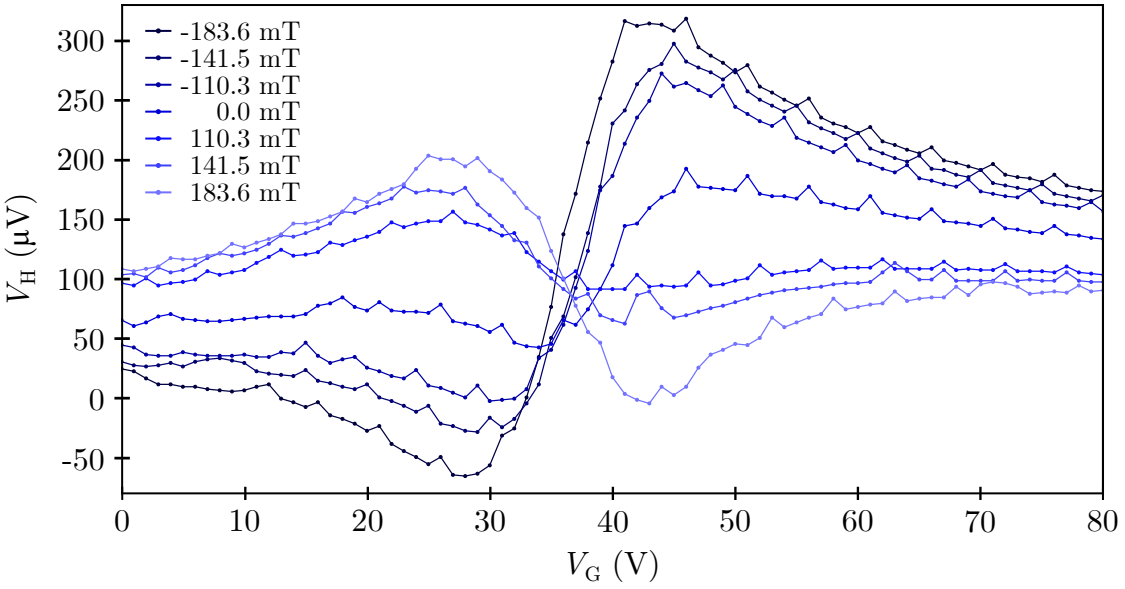


**Fig. 5.3:** Response of the constricted graphene Hall bar with SU-8 to various magnitudes and polarities of the magnetic field at $T = 30\,°\mathrm{C}$ upon application of gate voltage $V_G$. Clearly, a larger magnetic field generates a larger Hall voltage response. As expected, the sign of Hall voltage $V_H$ changes with the switch of the polarity of the applied magnetic field. However, there is also a small response without any field ($B = 0\,\mathrm{mT}$), which is referred to as offset Hall voltage. The asymmetry in the Hall voltage response, where $V_H = 0\,\mu\mathrm{V}$ does not correspond to $V_G \approx V_D$, is attributed to the presence of the offset voltage.

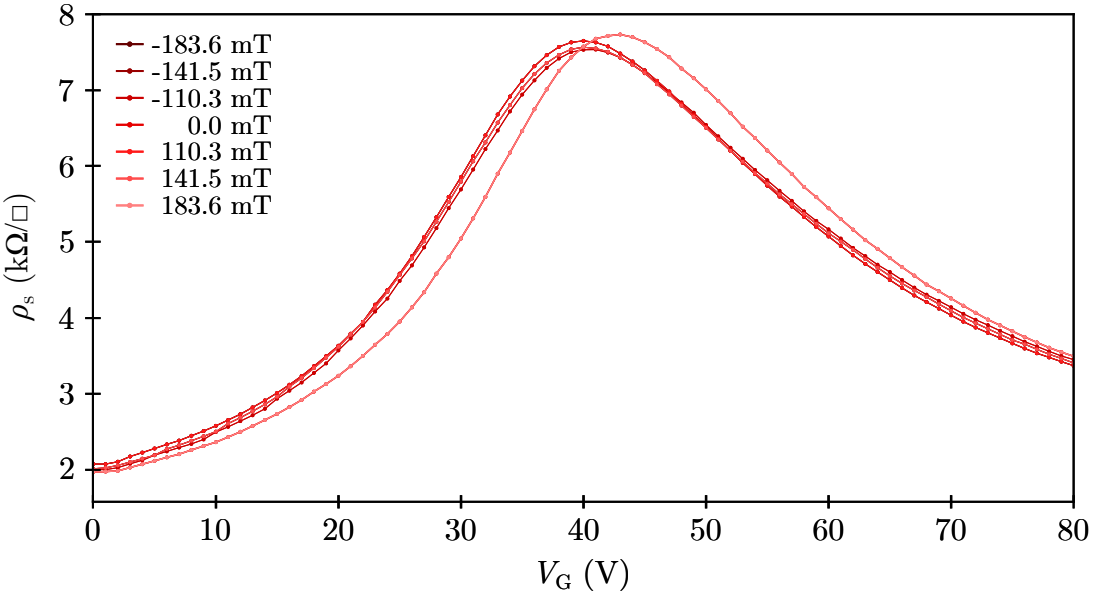


**Fig. 5.4:** Transfer curve of the constricted graphene Hall bar with SU-8 at various magnetic fields at $T = 30\,°C$. The sheet resistivity $\rho_s$ is independent of the magnetic field, as confirmed by the alignment of the peaks of the transfer curves. The slight shift of the transfer curve for $B = 183.6\,mT$ is likely caused by an imprecise temperature setting.

Fig. 5.4 serves as a confirmation that the sheet resistivity $\rho_s$, which is directly proportional to the longitudinal voltage $V$ according to Eq. 5.1, does not depend on the applied magnetic field. Although there is a slight shift of the peak of the transfer curve for $B = 183.6\,mT$, this can be assigned to an imprecise temperature setting rather than an effect induced by the magnetic field.

### 5.2.2 Influence of increasing temperature

One of the primary objectives of this thesis is to investigate the behaviour of graphene Hall probes based on FETs at elevated temperatures, which has not been systematically explored in previous studies. In this work, the graphene Hall elements are measured at intervals of 10 °C within a temperature range $T = (30–200)\,°C$ during each measurement cycle for a set magnetic field. Measurements at room temperature are carried out separately due to the prolonged cool-down time required to achieve $T = 25\,°C$.

Fig. 5.5 illustrates the effect of increasing temperature on the transfer curve of our graphene Hall probes. The peak of the $\rho_s(V_G)$ dependence, corresponding to the Dirac point in graphene, gradually moves to the right, indicating p-doping of the graphene layer. The peak value of sheet resistivity $\rho_s$ remains relatively constant until $T = 150\,°C$, above which it begins to decrease significantly. Moreover, the shape of the transfer curve stays consistent until $T = 150\,°C$ and then starts to noticeably widen for higher temperatures.

Next, the impact of temperature on the Hall voltage response is depicted in Fig. 5.6. Due to the dependency of the Hall voltage $V_H$ on the charge carrier density $n_{2D}$ (Eq. 2.7), the Hall voltage response also shifts to the right with increasing temperature in accordance with the shift of the transfer curve in Fig. 5.5. In connection to the change in transfer curves above $T = 150\,°C$, the Hall voltage response also seems to weaken considerably for high temperatures.

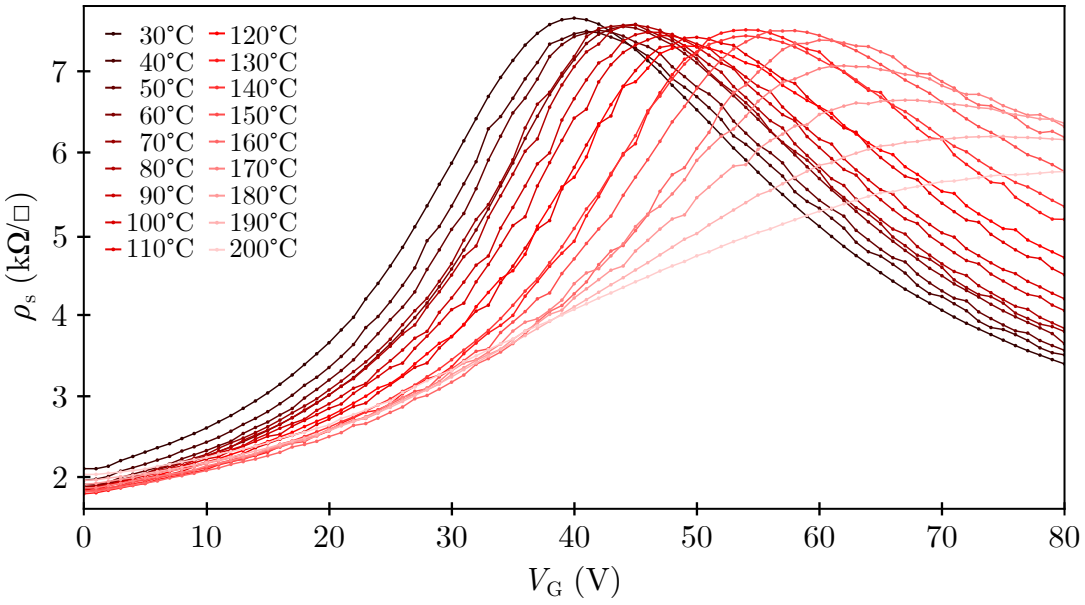


**Fig. 5.5:** Transfer curve of the constricted graphene Hall bar with SU-8 in a magnetic field $B = -183.6\,\mathrm{mT}$ for temperature range $T = (30\text{–}200)\,^\circ\mathrm{C}$. Increasing temperature causes a steady shift of the $\rho_s(V_G)$ dependence to the right, which indicates p-doping of the graphene Hall bar with temperature.

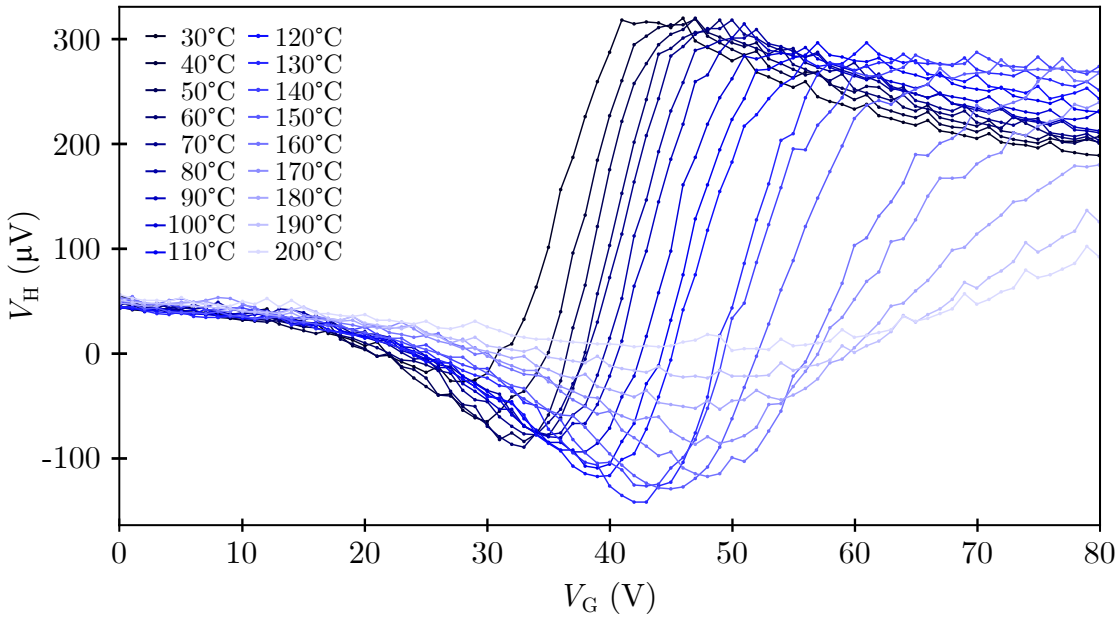


**Fig. 5.6:** Hall voltage response of the constricted graphene Hall bar with SU-8 to a magnetic field $B = -183.6\,\mathrm{mT}$ in a temperature range $T = (30\text{–}200)\,^\circ\mathrm{C}$. The gradual shift to the right with increasing temperature is explained by the dependence of the Hall voltage $V_H$ on the charge carrier density $n_{2D}$.

## 5.3 Discussion

### 5.3.1 Sensitivity of the graphene Hall probes

As mentioned in Sec. 2.3, the two parameters defining the sensitivity of graphene Hall probes are the Hall coefficient $R_H$ (Eq. 2.10) and the magnetic field detection limit $S_B^{1/2}$ (Eq. 2.11). In order to determine these values for our graphene Hall probes, we perform the following data processing: first, we filter our any significant noise peaks in the data; next, we interpolate the measured curves with cubic spline; and finally, we subtract the offset voltage spline from each Hall voltage spline. This procedure allows us to isolate the Hall voltage response only to the applied magnetic field without any offset. Fig. 5.7 demonstrates the results of this data processing on the measured data plotted in Fig. 5.3 for the constricted graphene Hall bar with SU-8 passivation layer at $T = 30\,°C$. After the offset correction, the interpolated data is symmetrical with $V_H = 0\,\mu V$ corresponding to $V_G \approx V_D$, which is consistent with the Hall effect.

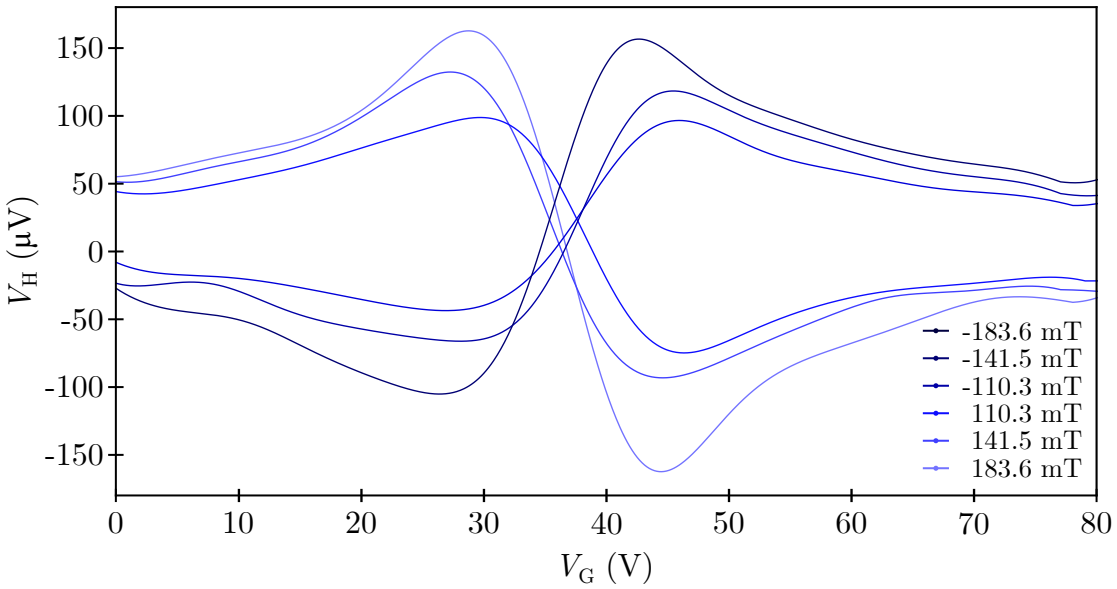


**Fig. 5.7:** Hall voltage response in varying magnetic fields to the application of gate voltage, interpolated using a cubic spline and corrected for offset. The intrepolated curves correspond to the measured data in Fig. 5.3 for the constricted graphene Hall bar with SU-8 at $T = 30\,°C$.

From the interpolated curves, we extract both extremes in the Hall voltage response for each magnetic field magnitude and polarity. The extreme in the $V_G < V_D$ part of the $V_H(V_G)$ dependence is facilitated by holes and in the $V_G > V_D$ range by electrons. Fig. 5.8 plots the extracted data points in the $V_G < V_D$ range as a function of the applied magnetic field, along with a linear fit of the data, as the $V_H(B)$ dependence should be linear following the Hall effect (Eq. 2.7). To determine the Hall coefficient $R_{H,max}$ according to Eq. 2.10, we use the slope of the linear fit as $\partial V_H/\partial B$. The calculated results of the Hall coefficient $R_{H,max}$ with holes as majority carriers for a graphene Hall bar with $w = 10\,\mu m$ and a constricted graphene Hall bar with SU-8 passivation layer on top are presented in Fig. 5.9a and b, respectively.

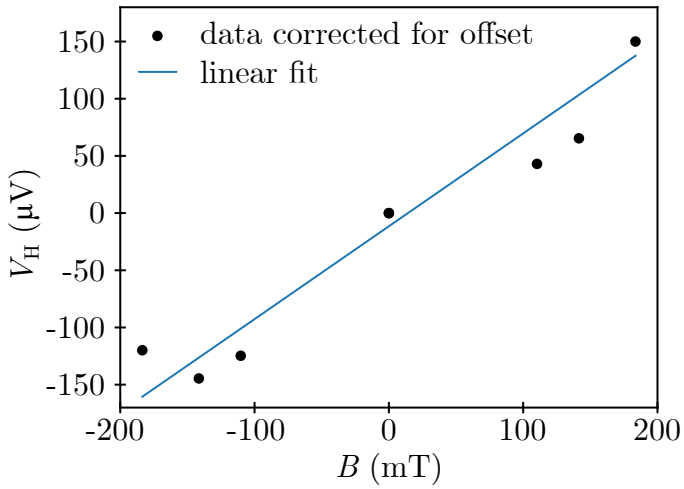


**Fig. 5.8:** Dependence of the maximum Hall voltage on the applied magnetic field. The data points are extracted from the interpolated $V_H(V_G)$ curves as extremes in the $V_G < V_D$ range.

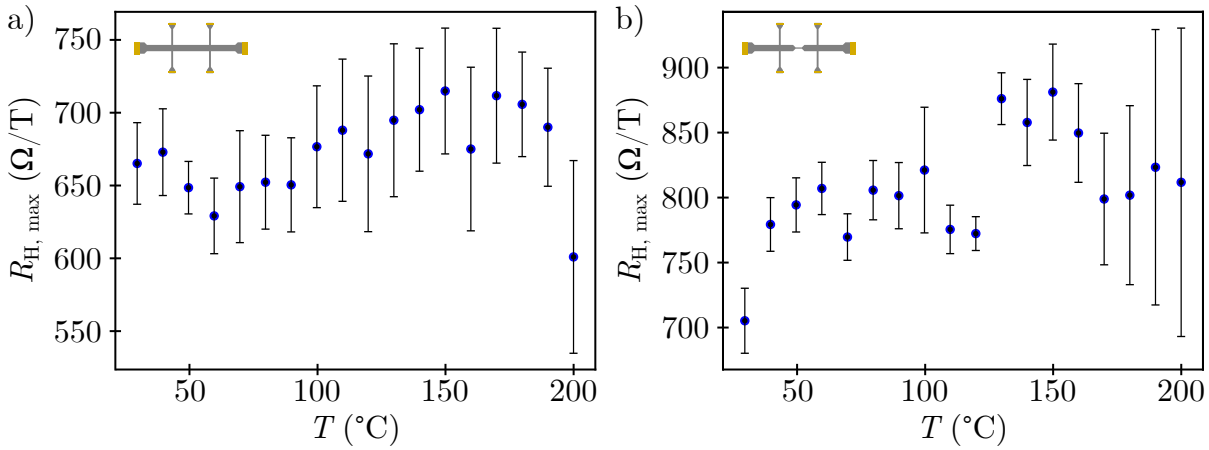


**Fig. 5.9:** Caption.

### 5.3.2 Mobility of charge carriers in graphene

### 5.3.3 The effect of temperature

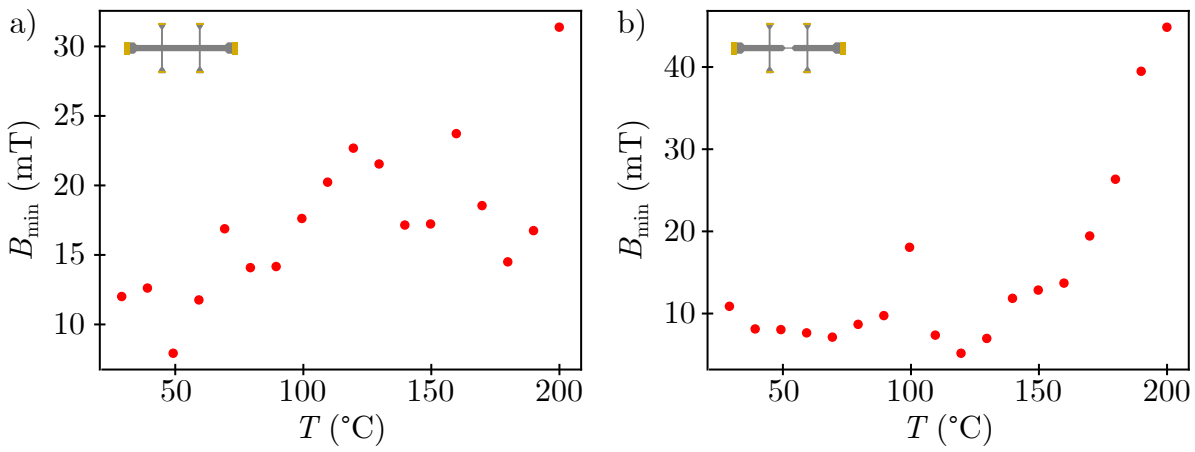


**Fig. 5.10:** Caption.

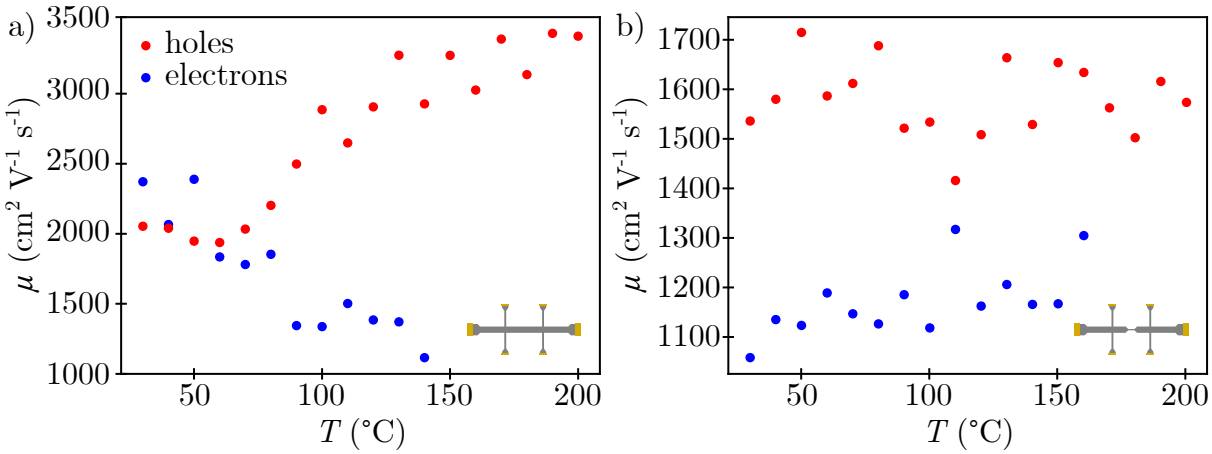


**Fig. 5.11:** Caption.

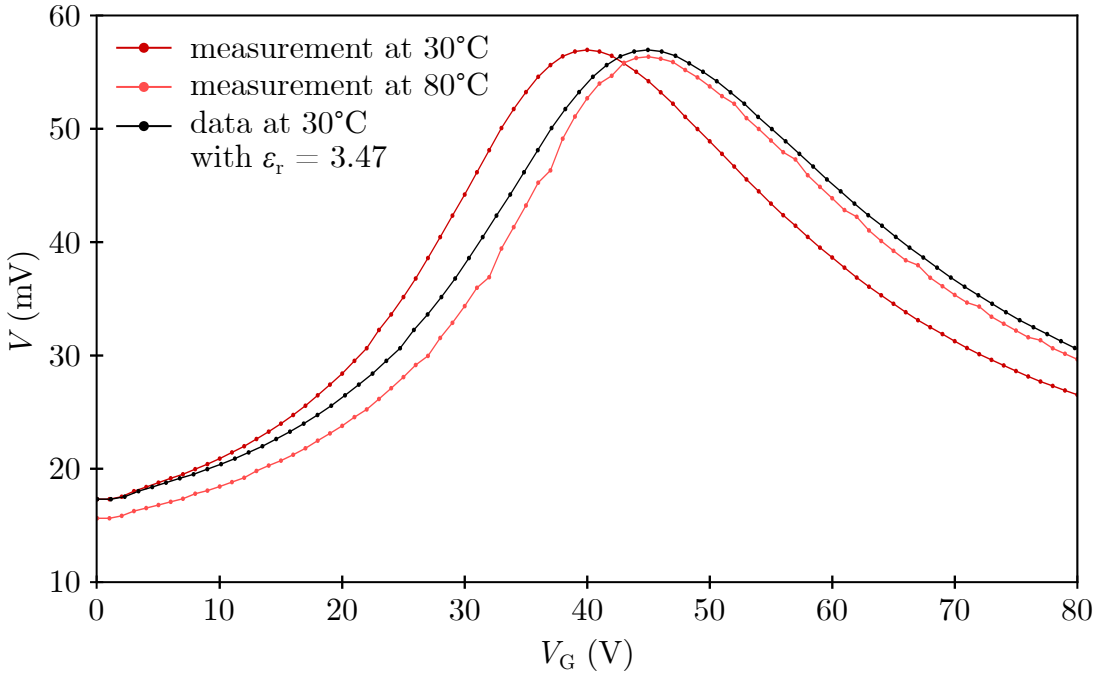


**Fig. 5.12:** Caption.

# Bibliography


[1] NOVOSELOV, K. S., A. K. GEIM, S. V. MOROZOV, D. JIANG, Y. ZHANG, S. V. DUBONOS, I. V. GRIGORIEVA a A. A. FIRSOV. Electric Field Effect in Atomically Thin Carbon Films. Science. 2004, 306(5696), 666-669. ISSN 0036-8075. Dostupné z: doi:10.1126/science.1102896

[2] KANG, S., D. LEE, J. KIM, A. CAPASSO, H. S. KANG, J.-W. PARK, C.-H. LEE a G.-H. LEE. 2D semiconducting materials for electronic and optoelectronic applications: potential and challenge. 2D Materials. 2020, 7(2). ISSN 2053-1583. Dostupné z: doi:10.1088/2053-1583/ab6267

[3] KUMBHAKAR, P., C. CHOWDE GOWDA a C. TIWARY. Advance Optical Properties and Emerging Applications of 2D Materials. Frontiers in Materials. 2021, 8. ISSN 2296-8016. Dostupné z: doi:10.3389/fmats.2021.721514

[4] AKINWANDE, D., C. J. BRENNAN, J. S. BUNCH, et al. A review on mechanics and mechanical properties of 2D materials—Graphene and beyond. Extreme Mechanics Letters. 2017, 13, 42-77. ISSN 23524316. Dostupné z: doi:10.1016/j.eml.2017.01.008

[5] SPLENDIANI, A., L. SUN, Y. ZHANG, T. LI, J. KIM, C.-Y. CHIM, G. GALLI a F. WANG. Emerging Photoluminescence in Monolayer MoS2. Nano Letters. 2010, 10(4), 1271-1275. ISSN 1530-6984. Dostupné z: doi:10.1021/nl903868w

[6] ZHU, B., H. ZENG, J. DAI a X. CUI. The Study of Spin-Valley Coupling in Atomically Thin Group VI Transition Metal Dichalcogenides. Advanced Materials. 2014, 26(31), 5504-5507. ISSN 09359648. Dostupné z: doi:10.1002/adma.201305367

[7] YANG, S., Y. CHEN a C. JIANG. Strain engineering of two-dimensional materials: Methods, properties, and applications. InfoMat. 2021, 3(4), 397-420. ISSN 2567-3165. Dostupné z: doi:10.1002/inf2.12177

[8] BUNCH, J. Scott, Scott S. VERBRIDGE, Jonathan S. ALDEN, Arend M. VAN DER ZANDE, Jeevak M. PARPIA, Harold G. CRAIGHEAD a Paul L. MCEUEN. Impermeable Atomic Membranes from Graphene Sheets. Nano Letters. 2008, 8(8), 2458-2462. ISSN 1530-6984. Dostupné z: doi:10.1021/nl801457b

[9] BALANDIN, Alexander A., Suchismita GHOSH, Wenzhong BAO, Irene CALIZO, Desalegne TEWELDEBRHAN, Feng MIAO a Chun Ning LAU. Superior Thermal Conductivity of Single-Layer Graphene. Nano Letters. 2008, 8(3), 902-907. ISSN 1530-6984. Dostupné z: doi:10.1021/nl0731872

[10] NAIR, R. R., P. BLAKE, A. N. GRIGORENKO, K. S. NOVOSELOV, T. J. BOOTH, T. STAUBER, N. M. R. PERES a A. K. GEIM. Fine Structure Constant Defines Visual Transparency of Graphene. Science. 2008, 320(5881), 1308-1308. ISSN 0036-8075. Dostupné z: doi:10.1126/science.1156965

[11] CASTRO NETO, A. H., F. GUINEA, N. M. R. PERES, K. S. NOVOSELOV a A. K. GEIM. The electronic properties of graphene. *Reviews of Modern Physics*. 2009, **81**(1), 109-162. ISSN 0034-6861. doi: 10.1103/RevModPhys.81.109

[12] BEENAKKER, C. W. J. Colloquium: Andreev reflection and Klein tunneling in graphene. Reviews of Modern Physics. 2008, 80(4), 1337-1354. ISSN 0034-6861. Dostupné z: doi:10.1103/RevModPhys.80.1337

[13] ZHANG, S. J., S. S. LIN, X. Q. LI, et al. Opening the band gap of graphene through silicon doping for the improved performance of graphene/GaAs heterojunction solar cells. Nanoscale. 2016, 8(1), 226-232. ISSN 2040-3364. Dostupné z: doi:10.1039/C5NR06345K

[14] HAN, M. Y., B. ÖZYILMAZ, Y. ZHANG a P. KIM. Energy Band-Gap Engineering of Graphene Nanoribbons. Physical Review Letters. 2007, 98(20). ISSN 0031-9007. Dostupné z: doi:10.1103/PhysRevLett.98.206805

[15] ZHOU, S. Y., G.-H. GWEON, A. V. FEDOROV, et al. Substrate-induced bandgap opening in epitaxial graphene. Nature Materials. 2007, 6(10), 770-775. ISSN 1476-1122. Dostupné z: doi:10.1038/nmat2003

[16] IHN, Thomas. Semiconductor Nanostructures: Quantum States and Electronic Transport. Oxford, New York: Oxford University Press, 2010. ISBN 978-0-19-953442-5 978-0-19-953443-2.

[17] ZIEGLER, K. Minimal conductivity of graphene: Nonuniversal values from the Kubo formula. Physical Review B. 2007, 75(23). ISSN 1098-0121. Dostupné z: doi:10.1103/PhysRevB.75.233407

[18] NOVOSELOV, K. S., A. K. GEIM, S. V. MOROZOV, D. JIANG, M. I. KATSNELSON, I. V. GRIGORIEVA, S. V. DUBONOS a A. A. FIRSOV. Two-dimensional gas of massless Dirac fermions in graphene. Nature. 2005, 438(7065), 197-200. ISSN 0028-0836. Dostupné z: doi:10.1038/nature04233

[19] SHARMA, P., J.S. GOMEZ-DIAZ, A. M. IONESCU a J. PERRUISSEAU-CARRIER. Determination of minimum conductivity of graphene from contactless microwaves measurements. 2012 12th IEEE International Conference on Nanotechnology (IEEE-NANO). IEEE, 2012, 2012, p. 1-4. ISBN 978-1-4673-2200-3. Dostupné z: doi:10.1109/NANO.2012.6322060

[20] TAN, Y.-W., Y. ZHANG, K. BOLOTIN, et al. Measurement of Scattering Rate and Minimum Conductivity in Graphene. Physical Review Letters. 2007, 99(24). ISSN 0031-9007. Dostupné z: doi:10.1103/PhysRevLett.99.246803

[21] MANZELI, S., D. OVCHINNIKOV, D. PASQUIER, O. V. YAZYEV a A. KIS. 2D transition metal dichalcogenides. Nature Reviews Materials. 2017, 2(8). ISSN 2058-8437. Dostupné z: doi:10.1038/natrevmats.2017.33

[22] YU, Young-Jun, Yue ZHAO, Sunmin RYU, Louis E. BRUS, Kwang S. KIM a Philip KIM. Tuning the Graphene Work Function by Electric Field Effect. Nano Letters. 2009, 9(10), 3430-3434. ISSN 1530-6984. Dostupné z: doi:10.1021/nl901572a

[23] PINTO, Hugo a Alexander MARKEVICH. Electronic and electrochemical doping of graphene by surface adsorbates. Beilstein Journal of Nanotechnology. 2014, 5, 1842-1848. ISSN 2190-4286. Dostupné z: doi:10.3762/bjnano.5.195

[24] WEHLING, T. O., K. S. NOVOSELOV, S. V. MOROZOV, E. E. VDOVIN, M. I. KATSNELSON, A. K. GEIM a A. I. LICHTENSTEIN. Molecular Doping of Graphene. Nano Letters. 2008, 8(1), 173-177. ISSN 1530-6984. Dostupné z: doi:10.1021/nl072364w

[25] LIU, H., Y. LIU a D. ZHU. Chemical doping of graphene. J. Mater. Chem. 2011, 21(10), 3335-3345. ISSN 0959-9428. Dostupné z: doi:10.1039/C0JM02922J

[26] LEE, H., K. PAENG a I. S. KIM. A review of doping modulation in graphene. Synthetic Metals. 2018, 244, 36-47. ISSN 03796779. Dostupné z: doi:10.1016/j.synthmet.2018.07.001

[27] KWON, Bitnuri, Hyeonhu BAE, Hoonkyung LEE, et al. Ultrasensitive N-Channel Graphene Gas Sensors by Nondestructive Molecular Doping. ACS Nano. 2022, 16(2), 2176-2187. ISSN 1936-0851. Dostupné z: doi:10.1021/acsnano.1c08186

[28] MISHRA, N., J. BOECKL, N. MOTTA a F. IACOPI. Graphene growth on silicon carbide: A review. Physica status solidi (a). 2016, 213(9), 2277-2289. ISSN 1862-6300. Dostupné z: doi:10.1002/pssa.201600091

[29] RUAN, M., Y. HU, Z. GUO, R. DONG, J. PALMER, J. HANKINSON, C. BERGER a W. A. DE HEER. Epitaxial graphene on silicon carbide: Introduction to structured graphene. MRS Bulletin. 2012, 37(12), 1138-1147. ISSN 0883-7694. Dostupné z: doi:10.1557/mrs.2012.231

[30] RUAN, Gedeng, Zhengzong SUN, Zhiwei PENG a James M. TOUR. Growth of Graphene from Food, Insects, and Waste. *ACS Nano*. 2011, **5**(9), 7601-7607. ISSN 1936-0851. doi: 10.1021/nn202625c

[31] LI, Xuesong, Weiwei CAI, Jinho AN, et al. Large-Area Synthesis of High-Quality and Uniform Graphene Films on Copper Foils. Science [online]. 2009, 324(5932), 1312-1314 [cit. 2022-11-16]. ISSN 0036-8075. Dostupné z: doi:10.1126/science.1171245

[32] YAN, Zheng, Jian LIN, Zhiwei PENG, et al. Toward the Synthesis of Wafer-Scale Single-Crystal Graphene on Copper Foils. ACS Nano. 2012, 6(10), 9110-9117. ISSN 1936-0851. Dostupné z: doi:10.1021/nn303352k

[33] WANG, Hong, Guanzhong WANG, Pengfei BAO, Shaolin YANG, Wei ZHU, Xing XIE a Wen-Jun ZHANG. Controllable Synthesis of Submillimeter Single-Crystal Monolayer Graphene Domains on Copper Foils by Suppressing Nucleation. Journal of the American Chemical Society. 2012, 134(8), 3627-3630. ISSN 0002-7863. Dostupné z: doi:10.1021/ja2105976

[34] LI, Xuesong, Carl W. MAGNUSON, Archana VENUGOPAL, Rudolf M. TROMP, James B. HANNON, Eric M. VOGEL, Luigi COLOMBO a Rodney S. RUOFF. Large-Area Graphene Single Crystals Grown by Low-Pressure Chemical Vapor Deposition of Methane on Copper. Journal of the American Chemical Society. 2011, 133(9), 2816-2819. ISSN 0002-7863. Dostupné z: doi:10.1021/ja109793s

[35] ZHANG, Yi, Lewis GOMEZ, Fumiaki N. ISHIKAWA, Anuj MADARIA, Koungmin RYU, Chuan WANG, Alexander BADMAEV a Chongwu ZHOU. Comparison of Graphene Growth on Single-Crystalline and Polycrystalline Ni by Chemical Vapor

Deposition. The Journal of Physical Chemistry Letters. 2010, 1(20), 3101-3107. ISSN 1948-7185. Dostupné z: doi:10.1021/jz1011466

[36] SUTTER, Peter, Jerzy T. SADOWSKI a Eli SUTTER. Graphene on Pt(111): Growth and substrate interaction. Physical Review B [online]. 2009, 80(24) [cit. 2022-11-16]. ISSN 1098-0121. Dostupné z: doi:10.1103/PhysRevB.80.245411

[37] CORAUX, Johann, Alpha T. N'DIAYE, Carsten BUSSE a Thomas MICHELY. Structural Coherency of Graphene on Ir(111). Nano Letters [online]. 2008, 8(2), 565-570 [cit. 2022-11-16]. ISSN 1530-6984. Dostupné z: doi:10.1021/nl0728874

[38] WANG, S M, Y H PEI, X WANG, et al. Synthesis of graphene on a polycrystalline Co film by radio-frequency plasma-enhanced chemical vapour deposition. Journal of Physics D: Applied Physics. 2010, 43(45). ISSN 0022-3727. Dostupné z: doi:10.1088/0022-3727/43/45/455402

[39] KWON, Soon-Yong, Cristian V. CIOBANU, Vania PETROVA, Vivek B. SHENOY, Javier BAREÑO, Vincent GAMBIN, Ivan PETROV a Suneel KODAMBAKA. Growth of Semiconducting Graphene on Palladium. Nano Letters. 2009, 9(12), 3985-3990. ISSN 1530-6984. Dostupné z: doi:10.1021/nl902140j

[40] ZHANG, Yi, Luyao ZHANG a Chongwu ZHOU. Review of Chemical Vapor Deposition of Graphene and Related Applications. Accounts of Chemical Research. 2013, 46(10), 2329-2339. ISSN 0001-4842. Dostupné z: doi:10.1021/ar300203n

[41] CUMMINGS, Aron W., Dinh Loc DUONG, Van Luan NGUYEN, Dinh VAN TUAN, Jani KOTAKOSKI, Jose Eduardo BARRIOS VARGAS, Young Hee LEE a Stephan ROCHE. Charge Transport in Polycrystalline Graphene: Challenges and Opportunities. Advanced Materials. 2014, 26(30), 5079-5094. ISSN 09359648. Dostupné z: doi:10.1002/adma.201401389

[42] YU, Qingkai, Luis A. JAUREGUI, Wei WU, et al. Control and characterization of individual grains and grain boundaries in graphene grown by chemical vapour deposition. Nature Materials. 2011, 10(6), 443-449. ISSN 1476-1122. Dostupné z: doi:10.1038/nmat3010

[43] HAO, Yufeng, M. S. BHARATHI, Lei WANG, et al. The Role of Surface Oxygen in the Growth of Large Single-Crystal Graphene on Copper. Science. 2013, 342(6159), 720-723. ISSN 0036-8075. Dostupné z: doi:10.1126/science.1243879

[44] YAN, Zheng, Jian LIN, Zhiwei PENG, et al. Toward the Synthesis of Wafer-Scale Single-Crystal Graphene on Copper Foils. ACS Nano. 2012, 6(10), 9110-9117. ISSN 1936-0851. Dostupné z: doi:10.1021/nn303352k

[45] PETRONE, Nicholas, Cory R. DEAN, Inanc MERIC, et al. Chemical Vapor Deposition-Derived Graphene with Electrical Performance of Exfoliated Graphene. Nano Letters. 2012, 12(6), 2751-2756. ISSN 1530-6984. Dostupné z: doi:10.1021/nl204481s

[46] GOEL, Naman, Aniket BABUTA, Abhimanyu KUMAR a Souvik GANGULI. Hall effect instruments, evolution, implications, and future prospects. Review of Scientific Instruments. 2020, 91(7). ISSN 0034-6748. Dostupné z: doi:10.1063/5.0009647

[47] COLLOMB, D., P. LI a S. BENDING. Frontiers of graphene-based Hall-effect sensors. Journal of Physics: Condensed Matter. 2021, 33(24). ISSN 0953-8984. Dostupné z: doi:10.1088/1361-648X/abf7e2

[48] DAI, Tongyu, Chengying CHEN, Le HUANG, Jianhua JIANG a Lian-Mao PENG. Ultrasensitive Magnetic Sensors Enabled by Heterogeneous Integration of Graphene Hall Elements and Silicon Processing Circuits. ACS Nano. 2020, 14(12), 17606-17614. ISSN 1936-0851. Dostupné z: doi:10.1021/acsnano.0c08435

[49] KITTEL, Charles. In: Introduction to solid state physics. 7th ed. New York: Wiley, 1996, s. 216-220. ISBN 0-471-11181-3.

[50] TAN, Y.-W., Y. ZHANG, H. L. STORMER a P. KIM. Temperature dependent electron transport in graphene. The European Physical Journal Special Topics. 2007, 148(1), 15-18. ISSN 1951-6355. Dostupné z: doi:10.1140/epjst/e2007-00221-9

[51] NOVOSELOV, K. S., Z. JIANG, Y. ZHANG, et al. Room-Temperature Quantum Hall Effect in Graphene. Science. 2007, 315(5817), 1379-1379. ISSN 0036-8075. Dostupné z: doi:10.1126/science.1137201

[52] BOLOTIN, K. I., K. J. SIKES, J. HONE, H. L. STORMER a P. KIM. Temperature-Dependent Transport in Suspended Graphene. Physical Review Letters. 2008, 101(9). ISSN 0031-9007. Dostupné z: doi:10.1103/PhysRevLett.101.096802

[53] HUANG, Le, Zhiyong ZHANG, Bingyan CHEN, Xiaomeng MA, Hua ZHONG a Lian-Mao PENG. Ultra-sensitive graphene Hall elements. Applied Physics Letters. 2014, 104(18). ISSN 0003-6951. Dostupné z: doi:10.1063/1.4875597

[54] HUANG, Le, Zhiyong ZHANG, Zishen LI, Bingyan CHEN, Xiaomeng MA, Lijun DONG a Lian-Mao PENG. Multifunctional Graphene Sensors for Magnetic and Hydrogen Detection. 2015, 7(18), 9581-9588. ISSN 1944-8244. Dostupné z: doi:10.1021/acsami.5b01070

[55] SONUSEN, S., O. KARCI, M. DEDE, S. AKSOY a A. ORAL. Single layer graphene Hall sensors for scanning Hall probe microscopy (SHPM) in 3–300K temperature range. Applied Surface Science. 2014, 308, 414-418. ISSN 01694332. Dostupné z: doi:10.1016/j.apsusc.2014.04.191

[56] IZCI, Davut, Carl DALE, Neil KEEGAN a John HEDLEY. The Construction of a Graphene Hall Effect Magnetometer. IEEE Sensors Journal. 2018, 18(23), 9534-9541. ISSN 1530-437X. Dostupné z: doi:10.1109/JSEN.2018.2872604

[57] WANG, Zhenxing, Luca BANSZERUS, Martin OTTO, Kenji WATANABE, Takashi TANIGUCHI, Christoph STAMPFER a Daniel NEUMAIER. Encapsulated graphene-based Hall sensors on foil with increased sensitivity. Physica status solidi (b). 2016, 253(12), 2316-2320. ISSN 03701972. Dostupné z: doi:10.1002/pssb.201600224

[58] XU, Huilong, Zhiyong ZHANG, Runbo SHI, Honggang LIU, Zhenxing WANG, Sheng WANG a Lian-Mao PENG. Batch-fabricated high-performance graphene Hall elements. Scientific Reports. 2013, 3(1). ISSN 2045-2322. Dostupné z: doi:10.1038/srep01207

[59] PETERS, A., S. TURVEY a A.B. HORSFALL. High Temperature Graphene Sensors for Harsh Environment Current Sensing. In: 2019 IEEE SENSORS. IEEE, 2019, 2019, s. 1-4. ISBN 978-1-7281-1634-1. Dostupné z: doi:10.1109/SENSORS43011.2019.8956693

[60] HE, H., N. SHETTY, T. BAUCH, S. KUBATKIN, T. KAUFMANN, M. CORNILS, R. YAKIMOVA a S. LARA-AVILA. The performance limits of epigraphene Hall sensors doped across the Dirac point. Applied Physics Letters. 2020, 116(22). ISSN 0003-6951. Dostupné z: doi:10.1063/5.0006749

[61] PANCHAL, V., K. CEDERGREN, R. YAKIMOVA, A. TZALENCHUK, S. KUBATKIN a O. KAZAKOVA. Small epitaxial graphene devices for magnetosensing applications. Journal of Applied Physics. 2012, 111(7). ISSN 0021-8979. Dostupné z: doi:10.1063/1.3677769

[62] PANCHAL, Vishal, Oscar IGLESIAS-FREIRE, Arseniy LARTSEV, Rositza YAKIMOVA, Agustina ASENJO a KAZAKOVA. Magnetic Scanning Probe Calibration Using Graphene Hall Sensor. IEEE Transactions on Magnetics. 2013, 49(7), 3520-3523. ISSN 0018-9464. Dostupné z: doi:10.1109/TMAG.2013.2243127

[63] GERKEN, Manuela, Aurélie SOLIGNAC, Davood MOMENI PAKDEHI, Alessandra MANZIN, Thomas WEIMANN, Klaus PIERZ, Sibylle SIEVERS a Hans Werner SCHUMACHER. Traceably calibrated scanning Hall probe microscopy at room temperature. Journal of Sensors and Sensor Systems. 2020, 9(2), 391-399. ISSN 2194-878X. Dostupné z: doi:10.5194/jsss-9-391-2020

[64] CIUK, Tymoteusz, Beata STANCZYK, Krystyna PRZYBOROWSKA, et al. High-Temperature Hall Effect Sensor Based on Epitaxial Graphene on High-Purity Semi-insulating 4H-SiC. IEEE Transactions on Electron Devices. 2019, 66(7), 3134-3138. ISSN 0018-9383. Dostupné z: doi:10.1109/TED.2019.2915632

[65] LI, Penglei, David COLLOMB, Zhen Jieh LIM, Sara DALE, Philippa SHEPLEY, Gavin BURNELL a Simon J. BENDING. High resolution magnetic microscopy based on semi-encapsulated graphene Hall sensors. Applied Physics Letters. 2022, 121(4). ISSN 0003-6951. Dostupné z: doi:10.1063/5.0097936

[66] KAZAKOVA, O., J.C. GALLOP, D.C. COX, E. BROWN, A. CUENAT a K. SUZUKI. Optimization of 2DEG InAs/GaSb Hall Sensors for Single Particle Detection. IEEE Transactions on Magnetics. 2008, 44(11), 4480-4483. ISSN 0018-9464. Dostupné z: doi:10.1109/TMAG.2008.2003507

[67] KOIDE, S, H TAKAHASHI, A ABDERRAHMANE, I SHIBASAKI a A SANDHU. High Temperature Hall sensors using AlGaN/GaN HEMT Structures. Journal of Physics: Conference Series. 2012, 352. ISSN 1742-6596. Dostupné z: doi:10.1088/1742-6596/352/1/012009

[68] COLLOMB, David, Penglei LI a Simon J. BENDING. Nanoscale graphene Hall sensors for high-resolution ambient magnetic imaging. Scientific Reports. 2019, 9(1). ISSN 2045-2322. Dostupné z: doi:10.1038/s41598-019-50823-8

[69] XU, Huilong, Le HUANG, Zhiyong ZHANG, Bingyan CHEN, Hua ZHONG a Lian-Mao PENG. Flicker noise and magnetic resolution of graphene hall sensors at low

frequency. Applied Physics Letters. 2013, 103(11). ISSN 0003-6951. Dostupné z: doi:10.1063/1.4821270

[70] POLLEY, Arup, Arul Vigneswar RAVICHANDRAN, Varun S. KUMAR, et al. Ambipolar Gate Modulation Technique for the Reduction of Offset and Flicker Noise in Graphene Hall-Effect Sensors. IEEE Sensors Journal. 2021, 21(22), 25675-25686. ISSN 1530-437X. Dostupné z: doi:10.1109/JSEN.2021.3115996

[71] KARPIAK, Bogdan, André DANKERT a Saroj P. DASH. Gate-tunable Hall sensors on large area CVD graphene protected by h-BN with 1D edge contacts. Journal of Applied Physics. 2017, 122(5). ISSN 0021-8979. Dostupné z: doi:10.1063/1.4997463

[72] TANG, Chiu-Chun, Ming-Yang LI, L. J. LI, C. C. CHI a J. C. CHEN. Characteristics of a sensitive micro-Hall probe fabricated on chemical vapor deposited graphene over the temperature range from liquid-helium to room temperature. Applied Physics Letters. 2011, 99(11). ISSN 0003-6951. Dostupné z: doi:10.1063/1.3640218

[73] SONG, Guibin, Mojtaba RANJBAR a Richard A. KIEHL. Operation of graphene magnetic field sensors near the charge neutrality point. Communications Physics. 2019, 2(1). ISSN 2399-3650. Dostupné z: doi:10.1038/s42005-019-0161-5

[74] SCHAEFER, Brian T., Lei WANG, Alexander JARJOUR, Kenji WATANABE, Takashi TANIGUCHI, Paul L. MCEUEN a Katja C. NOWACK. Magnetic field detection limits for ultraclean graphene Hall sensors. Nature Communications. 2020, 11(1), 4163. ISSN 2041-1723. Dostupné z: doi:10.1038/s41467-020-18007-5

[75] DAUBER, Jan, Abhay A. SAGADE, Martin OELLERS, Kenji WATANABE, Takashi TANIGUCHI, Daniel NEUMAIER a Christoph STAMPFER. Ultra-sensitive Hall sensors based on graphene encapsulated in hexagonal boron nitride. Applied Physics Letters. 2015, 106(19). ISSN 0003-6951. Dostupné z: doi:10.1063/1.4919897

[76] BLAKE, P., E. W. HILL, A. H. CASTRO NETO, K. S. NOVOSELOV, D. JIANG, R. YANG, T. J. BOOTH a A. K. GEIM. Making graphene visible. Applied Physics Letters. 2007, 91(6). ISSN 0003-6951. Dostupné z: doi:10.1063/1.2768624

[77] KRISHNA BHARADWAJ, B, Digbijoy NATH, Rudra PRATAP a Srinivasan RAGHAVAN. Making consistent contacts to graphene: effect of architecture and growth induced defects. Nanotechnology. 2016, 27(20). ISSN 0957-4484. Dostupné z: doi:10.1088/0957-4484/27/20/205705

[78] CHA, Jongin, Jangyup SON a Jongill HONG. A Bottom-Electrode Contact: The Most Suitable Structure for Graphene Electronics. Advanced Materials Interfaces. 2022, 9(6). ISSN 2196-7350. Dostupné z: doi:10.1002/admi.202102207

[79] ASTM International. Standard Test Methods for Measuring Resistivity and Hall Coeficient and Determining Hall Mobility in Single Crystal Semiconductors. Standard ASTM F76-08(2016)E1, 2016.

[80] Allresist. *Adhesion promoter AR 300-80 new.* Dostupné z: https://www.allresist.com/wp-content/uploads/sites/2/2021/02/Allresist_Product-information_Adhesions-Promoter_AR-300-80new_HMDS_English_web.pdf

[81] MicroChemicals. *Positive Tone Photoresists AZ 701 MiR Series*. Dostupné z: https://www.microchemicals.com/micro/tds_az_mir701_photoresist.pdf

[82] LI, Xuesong, Yanwu ZHU, Weiwei CAI, et al. Transfer of Large-Area Graphene Films for High-Performance Transparent Conductive Electrodes. Nano Letters. 2009, 9(12), 4359-4363. ISSN 1530-6984. Dostupné z: doi:10.1021/nl902623y

[83] Allresist. *Positive E-Beam Resists AR-P 6200 (CSAR 62)*. Dostupné z: https://www.allresist.com/wp-content/uploads/sites/2/2020/03/AR-P6200_CSAR62english_Allresist_product-information.pdf

[84] Kayaku Advanced Materials. *SU-8 2000 Permanent Negative Epoxy Photoresist*. Dostupné z: https://kayakuam.com/wp-content/uploads/2020/08/KAM-SU-8-2000-2000.5-2015-Datasheet-8.13.20-final.pdf

[85] MALARD, L.M., M.A. PIMENTA, G. DRESSELHAUS a M.S. DRESSELHAUS. Raman spectroscopy in graphene. Physics Reports. 2009, 473(5-6), 51-87. ISSN 03701573. Dostupné z: doi:10.1016/j.physrep.2009.02.003

[86] PENG, Zhiwei, Xiaolin CHEN, Yulong FAN, David J. SROLOVITZ a Dangyuan LEI. Strain engineering of 2D semiconductors and graphene: from strain fields to band-structure tuning and photonic applications. 2020, 9(1). ISSN 2047-7538. Dostupné z: doi:10.1038/s41377-020-00421-5

[87] THOMSEN, C. a S. REICH. Double Resonant Raman Scattering in Graphite. Physical Review Letters. 2000, 85(24), 5214-5217. ISSN 0031-9007. Dostupné z: doi:10.1103/PhysRevLett.85.5214

[88] MAULTZSCH, J., S. REICH a C. THOMSEN. Double-resonant Raman scattering in graphite: Interference effects, selection rules, and phonon dispersion. Physical Review B. 2004, 70(15). ISSN 1098-0121. Dostupné z: doi:10.1103/PhysRevB.70.155403

[89] GRAF, D., F. MOLITOR, K. ENSSLIN, C. STAMPFER, A. JUNGEN, C. HIEROLD a L. WIRTZ. Spatially Resolved Raman Spectroscopy of Single- and Few-Layer Graphene. Nano Letters. 2007, 7(2), 238-242. ISSN 1530-6984. Dostupné z: doi:10.1021/nl061702a

[90] DAS, A., S. PISANA, B. CHAKRABORTY, S. PISCANEC, S. K. SAHA, WAGHMARE a K. S. Nature Nanotechnology. 2008, 3(4). ISSN 1748-3387. Dostupné z: doi:10.1038/nnano.2008.67

[91] LIN, Yung-Chang, Chun-Chieh LU, Chao-Huei YEH, Chuanhong JIN, Kazu SUENAGA a Po-Wen CHIU. Graphene Annealing: How Clean Can It Be?. Nano Letters. 2012, 12(1), 414-419. ISSN 1530-6984. Dostupné z: doi:10.1021/nl203733r

[92] CASIRAGHI, C., S. PISANA, K. S. NOVOSELOV, A. K. GEIM a A. C. FERRARI. Raman fingerprint of charged impurities in graphene. Applied Physics Letters. 2007, 91(23). ISSN 0003-6951. Dostupné z: doi:10.1063/1.2818692

[93] Hirst Magnetic Instruments Ltd. *GM08 Gaussmeter with Transverse probe*. Dostupné z: https://www.gaussmeter.co.uk/index.php?route=product/download/download&did=18

[94] BARTOŠÍK, Miroslav, Jindřich MACH, Jakub PIASTEK, David NEZVAL, Martin KONEČNÝ, Vojtěch ŠVARC, Klaus ENSSLIN a Tomáš ŠIKOLA. Mechanism and Suppression of Physisorbed-Water-Caused Hysteresis in Graphene FET Sensors. ACS Sensors. 2020, 5(9), 2940-2949. ISSN 2379-3694. Dostupné z: doi:10.1021/acssensors.0c01441

# Symbols and abbreviations

**CMOS** complementary metal-oxide-semiconductor

**CVD** chemical vapour deposition

**EBL** electron beam lithography

**FET** field effect transistor

**hBN** hexagonal boron nitride

**HSQ** hydrogen silsesquioxane

**PMMA** poly(methyl methacrylate)

**RIE** reactive-ion etching

**SEM** scanning electron microscopy

**SiC** silicon carbide

**TMDCs** transition metal dichalcogenides

**UHV** ultra high vacuum